Monthly Notices of the ROYAL ASTRONOMICAL SOCIETY

MNRAS **512,** 6104–6121 (2022) https://doi.org/10.1093/mnras/stac880
Advance Access publication 2022 April 11

# Deep ASKAP EMU Survey of the GAMA23 field: properties of radio sources

Gülay Gürkan [1,2★] I. Prandoni [3★] A. O'Brien,[4,5,6] W. Raja,[5] L. Marchetti [3,7] M. Vaccari [3,8] S. Driver [9] E. Taylor,[10] T. Franzen,[11] M. J. I. Brown [12] S. Shabala [13] H. Andernach,[14] A. M. Hopkins,[15] R. P. Norris [5,6] D. Leahy [16] M. Bilicki [17] H. Farajollahi,[6] T. Galvin [18] G. Heald [2] B. S. Koribalski [5,6] T. An [19,20] and K. Warhurst[2]

*Affiliations are listed at the end of the paper*

Accepted 2022 March 26. Received 2022 March 26; in original form 2021 November 11

## ABSTRACT

We present the Australian Square Kilometre Array Pathfinder (ASKAP) observations of the Galaxy and Mass Assembly (GAMA)-23h field. The survey was carried out at 887.5 MHz and covers an ∼83 square deg field. We imaged the calibrated visibility data, taken as part of the Evolutionary Mapping of Universe Early Science Programme, using the latest version of the `ASKAPSoft` pipeline. The final mosaic has an angular resolution of 10 arcsec and a central rms noise of around 38 μJy beam$^{-1}$. The derived radio source catalogue has 39 812 entries above a peak flux density threshold of 5$\sigma$. We searched for the radio source host galaxy counterparts using the GAMA spectroscopic (with an *i*-band magnitude limit of 19.2 mag) and multiwavelength catalogues that are available as part of the collaboration. We identified hosts with GAMA spectroscopic redshifts for 5934 radio sources. We describe the data reduction, imaging, and source identification process, and present the source counts. Thanks to the wide area covered by our survey, we obtain very robust counts down to 0.2 mJy. ASKAP's exceptional survey speed, providing efficient, sensitive, and high-resolution mapping of large regions of the sky in conjunction with the multiwavelength data available for the GAMA23 field, allowed us to discover 63 giant radio galaxies. The data presented here demonstrate the excellent capabilities of ASKAP in the pre-SKA era.

**Key words:** catalogues – surveys – radio continuum: galaxies – radio continuum: general.

## 1 INTRODUCTION

In the extragalactic Universe, there are two main mechanisms producing non-thermal synchrotron emission: (i) relativistic magnetized plasma jets that are generated by the accretion of matter on to supermassive black holes (SMBHs) at the centre of jetted (or radio-loud) active galactic nuclei (AGNs) and (ii) cosmic ray electrons accelerated by supernova explosions, the end products of massive stars. The latter radio emission can be used as a probe of the recent number of massive stars and therefore as a proxy for the star formation rate (SFR; Condon 1992). There are other means for estimating SFRs of galaxies such as ultraviolet (UV) and infrared (IR) luminosity. UV measures are strongly affected by uncertainties due to dust obscuration corrections, whereas IR surveys are limited by poor resolution and source blending. Unlike the UV and IR, the radio emission from normal galaxies traces both obscured and unobscured star formation and is free of cirrus contamination that affects IR estimates at faint luminosities (Condon 1992). In the absence of deep X-ray observations, the luminosity (as well as morphology, spectrum, and polarization) of radio emission from jetted AGN provides us the only way of assessing the kinetic luminosity produced by the AGN (i.e. jet power; e.g. Willott et al. 1999), even though large uncertainties remain to be addressed (Kaiser, Dennett-Thorpe & Alexander 1997; Blundell & Rawlings 2000; Manolakou & Kirk 2002; Hardcastle & Krause 2013; Hardcastle 2018; Turner et al. 2018). AGN radio luminosity is generally expected to be much higher than the radio luminosity produced by star formation, at least for powerful jetted AGNs. In low-luminosity AGNs (at around $P < 10^{24}$ W Hz$^{-1}$), both processes might contribute to the radio emission at similar levels (e.g. Gürkan et al. 2018, 2019; Hartley et al. 2021; Macfarlane et al. 2021; McKean et al. 2021). Hence, the separation of these processes contributing to the total radio emission becomes a challenge. Sub-arcsec resolution radio data would assist us to separate these two processes, but obtaining this for significantly large samples is still challenging, though there is progress towards overcoming this (e.g. Morabito et al. 2022). Alternatively, one should rely on optical spectroscopy and/or multiwavelength photometric data. Wide-field, sensitive and high-resolution radio surveys in regions of the sky where optical spectroscopy and dense multiband data are available will be crucial for comprehending the evolution of AGNs (Best et al. 2014; Smolčić et al. 2017b; Ocran et al. 2021), the link between AGNs and their host galaxies (e.g. Gürkan et al. 2015; Webster et al. 2021; Mingo et al. 2022), the properties and evolution of star-forming galaxies (SFGs; e.g. Gürkan et al. 2018; Smith et al. 2021), and systematic

★ E-mail: ggurkan.astro@gmail.com (GG); isabella.prandoni@inaf.it (IP)

selection and investigation of rare radio sources (e.g. Gürkan et al. 2021).

Waiting for the Square Kilometre Array (SKA[1]) era, pathfinders and precursors of the SKA already expand the frontiers of astrophysical research by performing wide-field radio surveys. At the low end of the radio spectrum (50–300 MHz), recent radio surveys such as the Low Frequency Array (LOFAR; van Haarlem et al. 2013) Multifrequency Snapshot Sky Survey (Heald et al. 2015), the LOFAR Low-band antenna Sky Survey (de Gasperin et al. 2021), the LOFAR Two-metre Sky Survey (LoTSS; Shimwell et al. 2017, 2022), the GaLactic and Extragalactic All-Sky Murchison Wide-Field Array (MWA; Tingay et al. 2013) Survey (GLEAM; Hurley-Walker et al. 2017), and the TIFR Giant Metrewave Radio Telescope (GMRT; Swarup et al. 1991) 150 MHz all-Sky radio Survey (TGSS; Intema et al. 2017) have proven the impact of sensitive low-frequency radio observations in both galactic and extragalactic science. In the mid-frequency range (800 MHz to 2 GHz), successful wide-field radio surveys include the Sydney University Molonglo Sky Survey (SUMSS; Mauch et al. 2003), the 1.4 GHz National Radio Astronomy Observatory (NRAO) Very Large Array (VLA) Sky Survey (NVSS; Condon et al.1998), the Faint Images of the Radio Sky at Twenty Centimeters (FIRST; Becker, White & Helfand 1995), and the Karl G. Jansky Very Large Array Sky Survey (VLASS; Lacy et al. 2020).

As a survey instrument, the Australian SKA Pathfinder (ASKAP; Johnston et al. 2007; McConnell et al. 2016; Hotan et al. 2021) is capable of surveying wide sky fields rapidly with high resolution and sensitivity. ASKAP is located at the Murchison Radio-astronomy Observatory (MRO) in Western Australia, and is operated by the Commonwealth Scientific and Industrial Research Organisation (CSIRO). A full description of the array is provided by Hotan et al. (2021). Here, we only mention that ASKAP is an array of 36 12-m-diameter prime-focus antennas distributed over a 6 km-diameter region; each is equipped with an innovative phased-array feed (Hay et al. 2006) that enables the simultaneous digital formation of 36 dual-polarization beams to sample a field of view of up to 31 square deg. ASKAP can observe in the frequency range of 800–1800 MHz with an instantaneous bandwidth of 288 MHz. A shallow (about 250 net hours) ASKAP survey at 887.5 MHz (RACS; McConnell et al. 2020; Hale et al. 2021) has already completed its first phase. There is another ongoing radio continuum survey with ASKAP the 'Evolutionary Map of Universe' (EMU; Norris et al. 2011) to provide a deeper radio view of the full southern radio sky and up to +30 deg in the northern sky. EMU started its early science programme in 2018 and reached around 25 μJy beam$^{-1}$ root-mean-square (rms) noise at around 12 arcsec resolution (e.g. Joseph et al. 2019; Norris et al. 2021; Pennock et al. 2021).

The Galaxy and Mass Assembly (GAMA[2]; Driver et al. 2016) spectroscopic survey has collected spectra for ∼300 000 galaxies down to $r < 19.8$ mag over ∼286 deg$^2$. It was carried out using the AAOmega multi-object spectrograph on the Anglo-Australian Telescope by the GAMA team. One of the fields observed as part of GAMA is a 50 deg$^2$ region, centred at the right ascension $\alpha$J2000 = 23 h and the declination $\delta$J2000 = −32° and is referred to as GAMA23 (or G23). In G23, spectroscopy is limited to objects brighter than $i$ band = 19.2 mag.

G23 was observed as part of ASKAP commissioning (Leahy et al. 2019) and, later, as part of the EMU Early Science programme.

**Table 1.** Observation parameters.

| | |
|---|---|
| Frequency | 887.5 MHz |
| Bandwidth | 288 MHz |
| Integration per tile | 11 h |
| Footprint | square_6×6 |
| Beam (pitch) spacing | 0.9 deg |
| Area covered | 82.7 deg$^2$ |
| Angular resolution | 10 arcsec |

This region has also been observed by the far-IR (100–500 μm) instrument *Herschel Space Observatory* (H-ATLAS; Smith et al. 2017) and a few other key surveys such as *Wide-field Infrared Survey Explorer* (*WISE*; Wright et al. 2010), *Galaxy Evolution Explorer* (*GALEX*; Martin et al. 2003), the Kilo-Degree Survey (KiDS; de Jong et al. 2015), and the Visible and Infrared Survey Telescope for Astronomy (VISTA) Kilo-degree Infrared Galaxy (VIKING; Edge et al. 2013) survey. There is also a dedicated Australian Telescope Compact Array (ATCA) survey (GAMA Legacy ATCA Southern Survey) carried out at 5.5 and 9.5 GHz, providing radio data at much higher resolutions (e.g. Seymour et al. 2020). The field has also been targeted by the First Large Absorption Survey in H I early science programme (Allison et al. 2016) and provided upper limits on the H I column density frequency distribution function (Allison et al. 2020). The current data sets in conjunction with the imminent future surveys such as the Widefield ASKAP L-band Legacy All-sky Blind survey (Koribalski et al. 2020), the Polarization Sky Survey of the Universe's Magnetism survey (Gaensler et al. 2010), Deep Investigation of Neutral Gas Origins,[3] the Middle Ages Galaxy Properties with Integral Field Spectroscopy programme (Foster et al. 2021), and the upcoming observations with extended ROentgen Survey with an Imaging Telescope Array (e.g. Merloni, Nandra & Predehl 2020; Brunner et al. 2021), all covering the G23 field, will open further new windows and foster our understanding of the Universe.

In this paper, we describe the observations and re-imaging of EMU Early Science observations of the G23 field (Section 2). Assessment of the data quality is presented in Section 3. In Section 4, we describe our final data products and the sample properties, focusing on source counts and giant radio galaxies (GRGs). Our conclusions and future work are given in Section 5. Throughout the paper, we use the most recent Planck cosmology (Planck Collaboration VI 2020): $H_0 = 67.7$ km s$^{-1}$ Mpc$^{-1}$, $\Omega_m = 0.308$, and $\Omega_\Lambda = 0.692$. Spectral index $\alpha$ is defined in the sense $S \sim \nu^{-\alpha}$.

## 2 OBSERVATIONS, DATA REDUCTION, AND IMAGING

ASKAP observations (scheduling block identification number: 8132 and 8137) of the G23 field were carried out using the parameters given in Table 1 in 2019 March as part of the EMU Early Science project. During the observations 35 out of 36 antennas were operating. Observations were carried out using a rectangle tiling configuration. Each tile consists of 36 beams that were arranged as 6 by 6 with a beam spacing (pitch angle) of 0.9 deg. In order to cover the entire G23 region, two overlapping tiles (with a separation of 0.9 deg) were used (see Fig. 1 for design of a single tile).

The ASKAP data of the G23 field were reduced using `ASKAPSoft` (Version 0.24.0) in 2019. Detailed information about the ASKAP data processing can be found on the `ASKAPSoft` web

[1] https://www.skatelescope.org/
[2] http://www.gama-survey.org/
[3] https://dingo-survey.org/

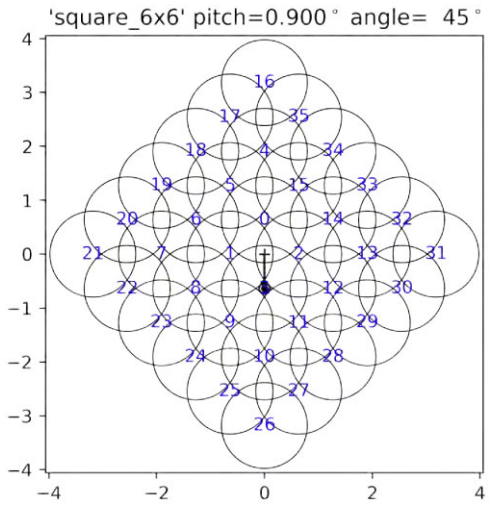


**Figure 1.** The arrangement of the 36 ASKAP beams in the 'square_6×6' configuration. The beams are numbered from 0 to 35.

page[4] (see also McConnell et al. 2020). Here, we briefly describe the steps taken in processing the data. As a first step, anomalous samples in the data from both calibrator and science fields were identified and removed. Frequency-dependent gains have been estimated using a primary flux calibrator (PKS B1934−638) for each beam, which were then used to set the instrumental flux-density scale and interferometer phase for each beam centre. Gridding and imaging of the calibrated multifrequency data for each beam (using a robust parameter of −0.5) have been done using `cimager` (version 1.0.1) in parallel processing on the Pawsey[5] computing cluster. A field model obtained for each beam as part of the imaging step has been used to perform self-calibration (this has been repeated twice). Images for each beam were made with a size of 4096 × 4096 pixels (each pixel is 2.5 arcsec). Standard continuum imaging parameters along with a Gaussian taper preconditioning (which allows to fit the beam while taking into account the restoring beam size defined by the user) were used to produce final images for each beam. The 36 final images were then primary beam corrected and mosaiced together in a single tile and the two resulting tile mosaics were further mosaiced together using the ASKAPSoft mosaicking function to generate the full radio map of the G23 field. The mosaicking function assumes a circular beam of full width at half-maximum (FWHM) $1.09\lambda/D$ for the primary beam model of the individual 36 beams. In addition, while combining individual beams, pixels whose primary beam gain is less than 20 per cent were disregarded. The final mosaic image has a 10 arcsec resolution and a central rms level of 38 μJy beam$^{-1}$ that is relatively smooth across the image. In Fig. 2, we show the rms noise map of the full mosaic and in Fig. 3 we show a histogram of noise estimates within the mosaic image. The red line shows the cumulative area of the mosaic with a noise less than a given value.

## 3 DATA QUALITY

### 3.1 Source extraction and flux scale assessment

The radio sources were extracted using the Python Blob Detector and Source Finder (PyBDSF; Mohan & Rafferty 2015). PyBDSF was run on the final mosaic using the parameters given in Table 2. The good surface brightness sensitivity of ASKAP allows us to observe several extended sources with a variety of morphologies. We utilize the `trous` wavelet module of PyBDSF that is designed to recover the low-surface brightness extended emission as much as possible. Briefly, the residual image that results from the fitting of Gaussian components is decomposed into wavelet images of various scales. This decomposition by the wavelet module aims to recover any extended emission that is not well fitted during Gaussian fitting. In practice, any remaining emission in the residual image can be further fitted by Gaussian functions whose size is tuned to the various wavelet scales. The PyBDSF parameters used for the source detection in our work were defined based on earlier works published in literature (e.g. Williams et al. 2019), and were fine-tuned by running some tests and evaluating the results of these tests. PyBDSF produces a catalogue of individual Gaussian components and a catalogue of sources. The latter is formed by grouping Gaussian components together, when they belong to the same 'island'. An island is defined as a region of adjacent pixels, where the flux is above a certain threshold. This allows PyBDSF to successfully combine components associated with the same source, as far as such components are nearby or overlapping. If source components are well separated, a visual inspection is necessary to identify them and merge them into a single multicomponent radio source (see Section 4.2). Both catalogues provide a number of source/component parameters. These include the position, integrated and peak flux density, structural parameters (measured and deconvolved sizes), and their estimated errors. The initial (raw) PyBDSF source catalogue consists of 54 814 sources with 40 186 objects having a peak flux density above a threshold of $5\sigma$.

In order to evaluate the accuracy of the mosaic flux scale, external radio catalogues from various surveys covering the G23 field were utilized. We particularly exploited all the available surveys, independent of their observing frequency. In this way, we avoid relying our comparison on a single survey and on a specific spectral index assumption. Following Sabater et al. (2021), we compared the flux densities of sources in common between our catalogue and catalogues from reference surveys, like SUMSS (Mauch et al. 2003), NVSS (Condon et al. 1998), TGSS (Intema et al. 2017), GLEAM (Hurley-Walker et al. 2017), and RACS (McConnell et al. 2020; Hale et al. 2021). Cross-matching of our source catalogue with external catalogues has been performed using different matching distances based on the spatial resolution of the comparison surveys. A number of constraints have been applied to external catalogues in order to eliminate possible biases that might be caused by the different effective depths and angular resolutions of the surveys. Parameters used for filtering and cross-matching are shown in Table 3. We initially selected isolated ASKAP sources (with a minimum distance to the nearest ASKAP source of 60 arcsec) in order to avoid contamination from neighbour sources. To avoid effects caused by different resolutions, the matching was limited to only compact ASKAP sources (i.e. size of deconvolved major axis <15 arcsec). In order to minimize incompleteness effects, only sources down to the completeness flux density limit of each comparison survey were taken into account. An additional survey-dependent minimum flux density threshold was applied. A further constraint was applied in the product of flux densities of the ASKAP measurement and each comparison survey because applying a flux density cut in only one of the reference surveys may introduce a bias towards sources with high absolute values of their spectral indices. We defined the threshold by multiplying the flux density of a source at the completeness limit of the comparison survey by the ASKAP flux density that such a source would have a spectral index of 1.5 at the ASKAP observing frequency

[4]https://www.atnf.csiro.au/computing/software/askapsoft
[5]https://pawsey.org.au/

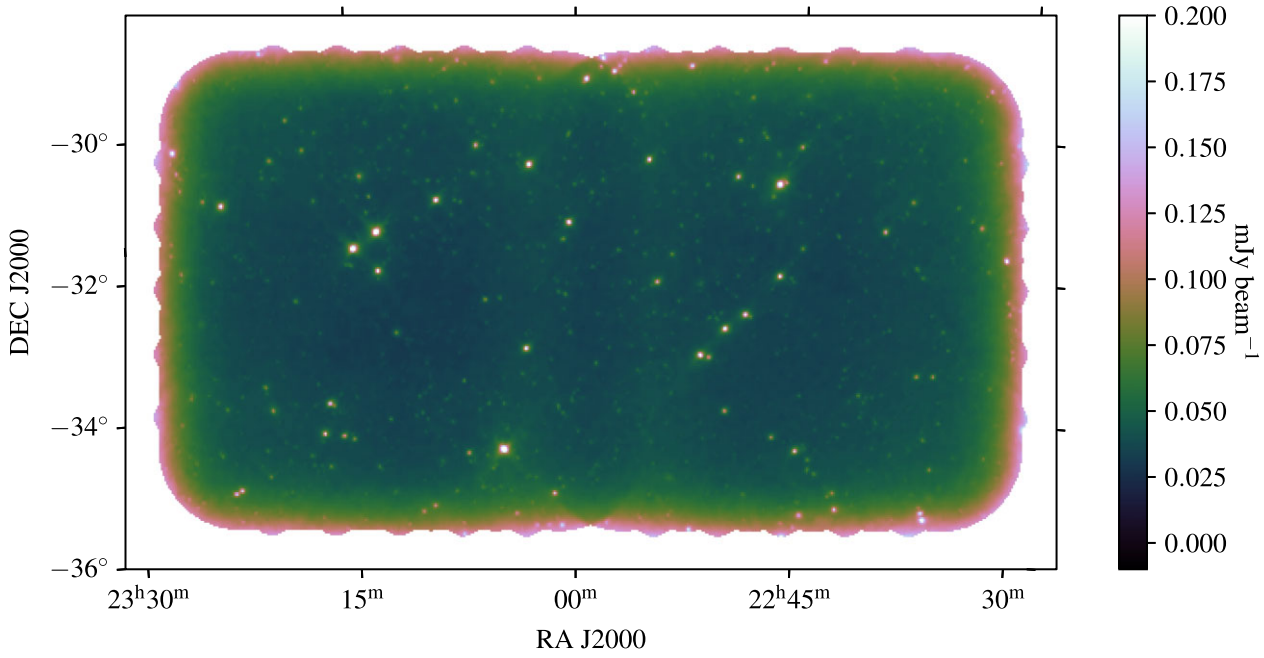


**Figure 2.** The rms noise map of the G23 ASKAP field. The noise map is produced as part of the source extraction process (see Section 3.1 for more details).

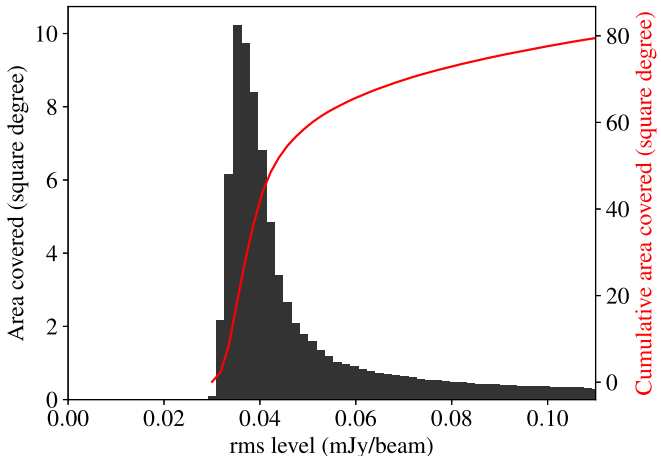


**Figure 3.** The histogram shows the distribution of the noise values in the noise map. The red line shows the cumulative area of the map with noise less than a given value.

**Table 2.** Key PyBDSF parameters that were used to obtain a catalogue of radio sources. `adaptive thresh` sets the signal-to-noise (SNR) above which sources may be affected by strong artefacts, `atrous jmax` gives the maximum order of the atrous wavelet decomposition, `group tol` is the tolerance parameter for grouping of Gaussians into sources, `rms box` sets the box size and step size for rms/mean map calculation, `rms box bright` sets the box size and step size for rms/mean map calculation near bright sources, and `thresh isl` determines the extent of island used for fitting.

| | |
|---|---|
| `adaptive thresh` | 150 |
| `atrous jmax` | 4 |
| `group tol` | 10 |
| `rms box` | (150, 15) |
| `rms box bright` | (60, 15) |
| `thresh isl` | 4 |

(887.5 MHz). The selected thresholds and completeness limits for all comparison surveys are listed in Table 3 and the illustration for two surveys is shown in Fig. 4. The maximum cross-match distance to the comparison survey was empirically determined based on the resolution of the matched survey (for lower resolution surveys, larger offset values were used).

Using the filtered sources, we estimated the median values of the ratios of ASKAP total flux densities to other survey flux densities and these are shown in Fig. 5. Errors in the median ratios were estimated using a bootstrapping technique. It is known that TGSS has region-dependent issues with the flux density scale (e.g. Intema et al. 2017). Therefore, we took into account the flux density uncertainty associated with a survey by adding it in quadrature to the error of the median of the flux density ratio. We used an Orthogonal Distance Regression (Boggs & Rogers 1990; Isobe et al. 1990) fit that takes

**Table 3.** Parameters used for the cross-match with external surveys and their filtering. The columns are, respectively, (1) survey name, (2) reference survey frequency, (3) resolution of the reference survey, (4) maximum cross-match distance for the survey, (5) survey completeness limit, (6) maximum size of the deconvolved major axis used for filtering, (7) value of the selection threshold in the product of the flux densities (see the text), and (8) number of sources selected after the cross-match and filtering.

| Survey | Survey frequency | Survey resolution (arcsec) | Max. cross-match radius (arcsec) | Survey flux density limit (mJy) | Max. major axis size (arcsec) | Flux product threshold (mJy) | N |
|---|---|---|---|---|---|---|---|
| NVSS | 1.4 GHz | 45 | 7 | 2 | 15 | 3.963 | 1410 |
| SUMSS | 843 MHz | 45 | 7 | 10 | 15 | 9.257 | 454 |
| TGSS | 150 MHz | 25 | 6 | 30 | 15 | 2.084 | 545 |
| RACS | 887.5 MHz | 25 | 6 | 1 | 15 | 1.000 | 226 |
| GLEAM | 200 MHz | 130 | 20 | 50 | 20 | 5.349 | 486 |

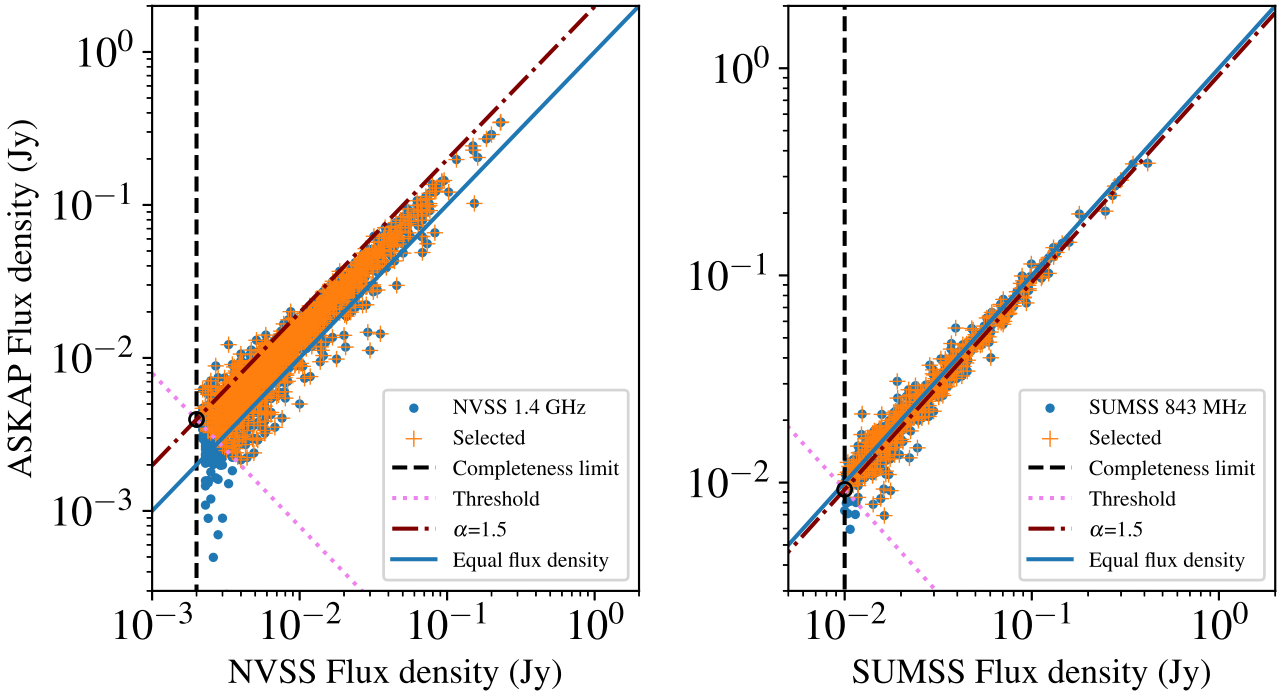


**Figure 4.** Selection of sources for the cross-match for the NVSS 1.4 GHz (left-hand panel) and the SUMSS 843 MHz (right-hand panel) samples. All the cross-matched sources are shown as blue dots and the selected ones after various filtering are marked with an orange cross. The survey's completeness limit is shown as a vertical dashed line. The line at which the flux densities are equal is shown as a solid blue line. The locus of sources with a spectral index of 1.5 is shown as a dash–dotted maroon line. The point at which this line and the survey completeness line cross is used as a reference for the selection threshold in the product of flux densities (see the text), which is marked as a pink dotted line.

into account the uncertainties in the ratios to estimate the flux density scale ratio as a function of frequency. Using the values obtained from the fitting process, we obtained a ratio of 1.016 (±0.11) at 887.5 MHz. As can also be seen in Fig. 5, our current flux density scale is very close to the best-fitting line (the dotted maroon line in Fig. 5). It is reassuring that overall our flux densities agree well with those of all the other surveys, including those undertaken at nearby frequencies, such as RACS and SUMSS. In particular, SUMSS fluxes are in perfect agreement with ours, while the discrepancy with RACS is around 5 per cent. This level of discrepancy is fully acceptable, given that the RACS survey shows position-dependent flux scale offsets up to 20 per cent, when compared with SUMSS (Hale et al. 2021; see their fig. 10). Since the offset from the best-fitting line is only 2 per cent, we do not further scale the flux density of our G23 sources.

### 3.2 Astrometric precision

In order to evaluate the astrometric precision of ASKAP source positions, we cross-matched the initial PyBDSF catalogue with various radio survey catalogues and the GAMA optical catalogue and calculated the positional offsets. These offsets are reported in Table 4. The astrometry of GAMA is tied to the KiDS survey in the G23 field. KiDS has internal astrometric error <0.03 arcsec (de Jong et al. 2013) and more robust than any other reference radio survey used in this work. The median ASKAP-GAMA position offsets are around 0.2 and 0.1 arcsec for RA and Dec., respectively (see Table 4). We applied these offsets to the source positions in order to bring our sources to a better agreement with the GAMA survey. While PyBDSF estimates uncertainties in source positions using the method given by Condon (1997), these still can be underestimated (e.g. Condon 2015). To further evaluate uncertainties in source positions, we select

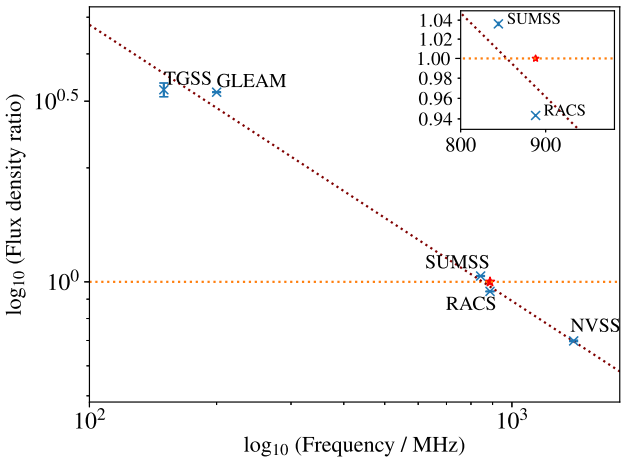


**Figure 5.** The median ratio of ASKAP total flux density to other survey total flux density is shown as a function of frequency of the surveys used for the cross-matching. The red star indicates the current ASKAP flux scale and the orange dotted line shows a ratio of unity, whereas the maroon dotted line shows the best fit to the data points. The inner panel shows a zoomed version of the plot in the 800–1000 MHz range.

bright and compact radio sources and estimate the angular separation from their hosts (see Section 4.2), in both RA and Dec. The error in the mean separation is around 0.6 arcsec for both RA and Dec. and this may be a better representation of the uncertainty in radio source positions.

### 3.3 Completeness, reliability, and bandwidth smearing

EMU Early Science observations of the G23 field were carried out with a frequency resolution of 1 MHz, so some level of bandwidth smearing is expected, causing an underestimation of the source peak flux density and a corresponding overestimation of source sizes in the radial direction such that the integrated flux density remains unchanged. Bandwidth smearing increases with the angular distance from the pointing centre of phase and depends on the bandpass width, the observing frequency, and the synthesized beam size. In a single ASKAP beam, the peak flux reduction due to bandwidth smearing is expected to increase radially to around 8 per cent at ∼1.7 deg angular distance from the phase centre (i.e. at a distance equal to the FWHM of the primary beam). The observations were done with a beam spacing of 0.9 deg. Such a spacing yields a uniform sensitivity across the observed region, when all beams are mosaiced together in a tile. The mosaicking consists of a weighted linear combination of the pixels of the overlapping beams, where the weights are estimated by taking into account beam response curves and local noise. As extensively discussed by Prandoni et al. (2000), such a combination results in a nearly uniform smearing across the mosaic (or tile). In other words, the radial dependence tends to cancel out, due to the fact that pixels at different distance from their respective beam centre are summed up. As demonstrated by Prandoni et al. (2000), the expected smearing in the mosaic should be of the order of the one expected for sources located at maximum distance from the closest beam centre, corresponding to $0.9\sqrt{2}/2 \sim 0.64$ deg in our case (see Prandoni et al. 2000, for more details). We then expect an ∼2 per cent reduction in the peak flux density due to smearing across the observed region.

In order to better characterize the sources and evaluate completeness of the survey, we carried out Monte Carlo simulations in the image plane. Point sources at random positions were injected in the residual map produced by PyBDSF (this ensures that the noise and its spatial distribution are consistent with those of the real data), and were recovered with PyBDSF using the same set of parameters as used for the real cataloguing. We chose the injected source flux densities randomly, using a power-law slope, spanning the range of observed flux densities in the survey (starting from 0.0001 Jy). We carried out 10 sets of simulations for each range of input source flux densities, using around 24 000 sources per run to improve the statistics. In the left-hand panel of Fig. 6, we show the flux density ratio of total flux to peak flux of recovered sources as a function of signal-to-noise ratio (SNR). For point sources, the ratio of total to peak flux density is expected to be unity and the observed spread around unity is due to measurements errors. We determined the 99 per cent envelope by fitting the 99th percentile in 20 logarithmic bins across the range of SNRs (seen as black open circles in the left-hand panel) using the simulated sources. The fitted envelope is described by the function $1.03 \pm 0.007 + 15.01 \pm 1.77/\mathrm{SNR}^{1.62 \pm 0.07}$ (black solid line in the left-hand panel of Fig. 6). It is clear that the total-to-peak flux density ratio of the simulated point sources tends to a value higher than unity (∼1.03) for high SNRs. Our investigation showed that this is due to the fact that the detection algorithm (PyBDSF) tends to overestimate the sizes of point sources. By repeating this analysis on the real source catalogue, we find that the total-to-peak flux density ratio tends to a slightly higher value (1.05) for large SNRs, and is better represented by the modified envelope $1.05 + 15.01/\mathrm{SNR}^{1.62}$ (see red dashed line in the right-hand panel of Fig. 6). This extra 2 per cent offset is fully consistent with the expected bandwidth smearing, but we cannot exclude some contribution from possible residual phase errors due to the lack of implementation of direction-dependent calibration (e.g. Wilber et al. 2020). We also note that we examined the total-to-peak flux density ratio of high-signal-to-noise point-like sources in different regions of the mosaic, and found no systematic trends across the mosaic. We utilize the envelope function shown in the right-hand panel of Fig. 6 to identify reliably resolved sources. All sources below that function are considered to be unresolved. Sources with multiple components (i.e. extended sources), obtained as part of the visual inspection (see Section 4.1), are shown as orange stars. All of them are above the envelope, as expected.

We have estimated the completeness of the catalogue (i.e. the probability that all sources above a given flux density are detected) by computing the fraction of detected sources in our simulation as a function of total flux density and integrating the detected fraction upwards from a given flux density limit. The detection fraction of sources as a function of total flux density is shown as a black line in the left-hand panel of Fig. 7. This detection fraction is expected to be largely driven by the variation in rms across the image (visibility area – the fraction of the image over which a source of a given flux density should be detectable). The number of detected sources as a function of sources that could be detected, accounting for the visibility area, is also shown in the left-hand panel as the purple line. The results of the completeness analysis (that takes into account the visibility function) are shown in the right-hand panel of Fig. 7. The catalogue is expected to be 90 per cent complete above 0.5 mJy for point sources. The source peak flux densities are reduced due to smearing (while total flux densities are not affected by the smearing effect). This will introduce additional incompleteness in the catalogue, as source detection is based on signal-to-noise thresholds ($\mathrm{SNR} = S_{\mathrm{peak}}/\sigma$). Considering that smearing is expected to be around 2 per cent, we expect extra incompleteness at SNR $<5.1\sigma$).

The reliability of a source catalogue can be defined as the probability that all sources above a given total flux density are

**Table 4.** Median astrometric offset from other reference surveys and the bootstrap errors of these offsets for RA and Dec., respectively.

| Surveys | Survey resolution (arcsec) | RA offset (arcsec) | Dec. offset (arcsec) | Error on median RA | Error on median DEC |
|---|---|---|---|---|---|
| GAMA | 2 | −0.18 | 0.1 | 0.008 | 0.006 |
| NVSS | 45 | −0.48 | −0.11 | 0.04 | 0.05 |
| SUMSS | 45 | 0.33 | −0.16 | 0.11 | 0.1 |
| RACS | 25 | −0.005 | −0.008 | 0.003 | 0.003 |
| TGSS | 25 | −0.29 | −0.28 | 0.04 | 0.06 |
| GLEAM | 130 | −0.90 | −3.04 | 0.27 | 0.23 |

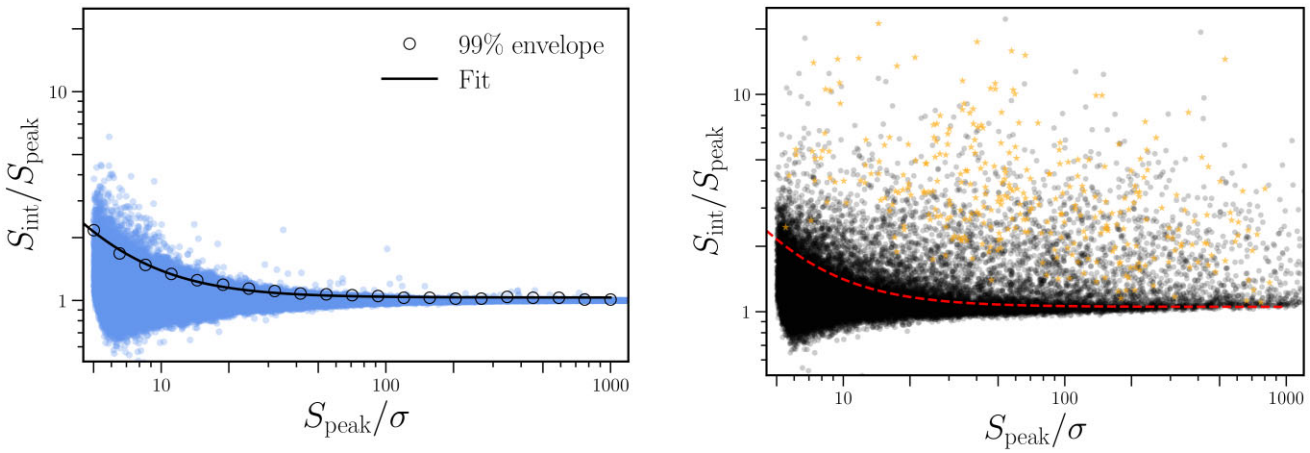


**Figure 6.** Left: Flux density ratio of the total flux to peak flux of simulated sources as a function of SNR. The black points show the threshold below which 99 per cent of the sources lie in 20 SNR bins. The black line shows a fit to this upper envelope. Right: Flux density ratio of the total flux to peak flux of sources in the source catalogue as a function of SNR. The red dashed line shows the modified version of the fitted envelope (see the text) and orange stars are multicomponent sources that are identified via visual inspection. Below, the red line sources are defined to be unresolved and as expected all multicomponent (i.e. resolved) sources are above this line.

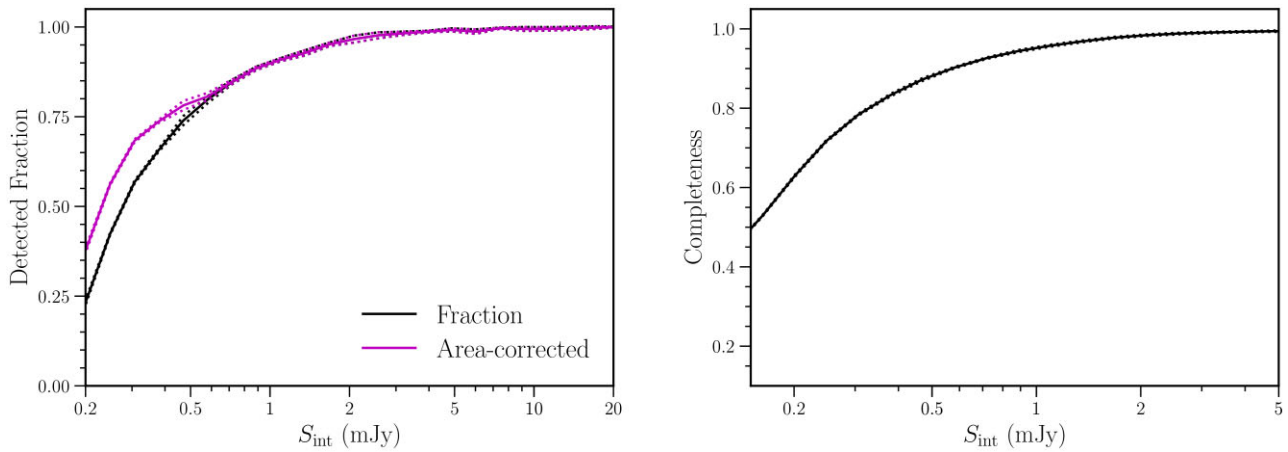


**Figure 7.** Results of the Monte Carlo completeness simulations. Left: Fraction of sources detected as a function of total flux density. The purple curve shows the detected fraction correcting for the effect of the visibility area. Right: Results of the completeness analysis. The dotted lines in both panels show the $1\sigma$ uncertainties.

real. In order to estimate the reliability, we extracted sources from the inverted residual mosaic image (assuming that negative image background features are statistically the same as positive ones). The detected negative 'sources' were grouped by total flux density into 20 logarithmic bins and these were compared to the binned results of the positive (i.e. detected in the mosaic by a regular source extraction process; see Section 3.1) sources. For our positive sources, we use the initial catalogue. The real number of sources is defined to be the number of positive sources after extracting the number of negative sources. This analysis showed that the reliability is >90 per cent

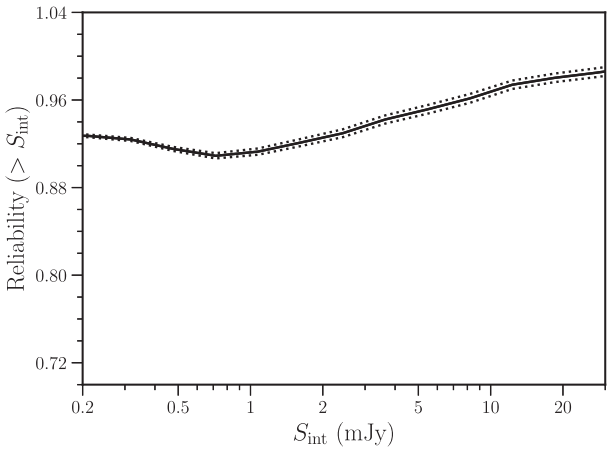


**Figure 8.** Results of the estimated reliability of the catalogue as a function of integrated flux density limit. Here, the reliability is defined as the probability that all sources above a given total flux density are real. The reliability is > 90 per cent over the entire flux density range. The dotted lines show the $1\sigma$ uncertainties.

down to that faintest flux densities. Fig. 8 shows the reliability curve determined from the number ratio of real sources over positive sources above a given total flux density.

It is worth noting that the completeness and reliability analyses were carried out for point sources only because at the faint end of the catalogue, where the effects of completeness and reliability are important, a large fraction of the sources are point-like. Taking into account the modified envelope (see Fig. 6, right-hand panel), 70 per cent are point-like below 1 mJy (i.e. at the fluxes where we see incompleteness). We expect spurious sources associated with noise peak detections to be point-like and dominate close to the detection threshold. Artefacts around bright sources may not be point like and would contribute to the curve given in Fig. 8 at fluxes larger than 1 mJy (and they were indeed removed; see Section 4.2).

## 4 FINAL DATA PRODUCTS AND SAMPLE PROPERTIES

### 4.1 Multiwavelength data and catalogues

This paper uses a multiwavelength catalogue to identify the host galaxies of radio sources as described in Section 4.2. The multiwavelength catalogue has been created by combining together different data products made available by the GAMA collaboration (Driver et al. 2011) that granted us advanced access to the GAMA DR4 catalogues (Driver et al. 2022). To construct our multiwavelength catalogue, we combined the following GAMA catalogues: the photometric catalogue `KidsVikingGAMAV01` produced with the `ProFound` image analysis package (Robotham et al. 2018) described by Bellstedt et al. (2020), the spectroscopic redshifts catalogue `SpecObjv27` (Liske et al. 2015), and the spectroscopic line measurements from the `GaussFitSimplev05` and `GaussFitComplexv05` catalogues (Gordon et al. 2017). The combination of these GAMA products provided a catalogue with (i) *GALEX* FUV and NUV, (ii) VST KiDS *u*, *g*, *r*, and *i*, (iii) AllWISE 3.4, 4.6, 12, and 22 μm, and (iv) *Herschel* SPIRE 250 350, and 500 μm photometric band information and spectroscopic information with a 95 per cent completeness down to the VST KiDS *i* magnitude of 19.2 (Liske et al. 2015), whereas this limit is $i < 22.25$ for the photometric sample.

The aforementioned catalogue was used to define a reliable sample of galaxies and AGNs to be used for our source identifications and provided all the information needed to characterize radio sources with host galaxy counterparts as described in Section 4.4. In order to remove the spurious sources and artefacts, we followed the instructions provided by Bellstedt et al. (2020). Since some radio galaxies may appear as star-like object in the optical, we did not remove stars from the GAMA catalogue but we flagged these objects as star-like or galaxy-like using two classification methods given by Baldry et al. (2012) and Bourne et al. (2016). This information assisted us in eliminating radio sources with host galaxies that are flagged as stars.

We also use photometric redshifts where spectroscopic redshifts are not available. To this end, we exploit two photometric redshift catalogues: a photometric redshift (photo-*z*) catalogue provided by the HELP collaboration (Shirley et al. 2021) and (ii) a catalogue of photometric redshifts estimated as part of our collaboration (`gkvEAZYPhotozv02`, joined with the rest of the GAMA DR4 data products). We prioritize using the HELP catalogue for the reasons outlined below. The HELP catalogue provides reliable photo-*z*s for the sources that lack spectroscopic information. The HELP photo-*z*s are estimated using a public photometric redshift code EAZY (Brammer, van Dokkum & Coppi 2008) and following the methods described by Duncan et al. (2018a, b). Briefly, the EAZY algorithm proceeds through a grid of redshifts defined by a user, and at each redshift it finds the best-fitting synthetic template spectral energy distributions (SEDs) by minimizing the $\chi^2$ goodness-of-fit parameter for every valid combination. The posterior probability density function (PDF) for redshift is then derived by considering the likelihood associated with the best-fitting template at each redshift, optionally with magnitude-dependent prior. The HELP collaboration uses different template sets: (i) stellar-only templates and (ii) the EAZY default library, two other sets including both stellar and AGN/quasar contributions and the SED templates by Brown et al. (2014). In the estimation of photometric redshifts, the HELP collaboration utilizes either SED templates or machine-learning estimates. This produces a hybrid consensus photo-*z* estimate with accurately calibrated uncertainties. They also treat separately the known AGN samples (identified using optical, IR, and X-ray data) to obtain better estimates of AGN photometric redshifts.

For the sources whose redshifts are not available in either catalogues mentioned earlier, we then make use of a photometric redshift catalogue produced as part of our collaboration using the EAZY software. For this, we used the atlas of 129 empirical galaxy spectra by Brown et al. (2014) as a template set. Since we do not treat AGNs separately, photometric redshifts for sources where AGN emission dominates the observed optical–NIR spectrum might not be completely reliable. For a more comprehensive description of the multiwavelength catalogues and multiwavelength analysis of the radio sources, we refer the reader to Marchetti et al. (in preparation).

### 4.2 Source association, host galaxy identification, and final catalogue

The initial radio source catalogue was processed in order to clean it from spurious sources and to reliably associate separate components belonging to the same source. To identify artefacts around bright sources, we filtered the bright compact sources with multiple neighbouring sources, and visually inspected them. Confirmed artefacts were then removed from the catalogue. Then, the source association and optical identification processes were carried out in parallel. As mentioned earlier for the host galaxy source identification, we

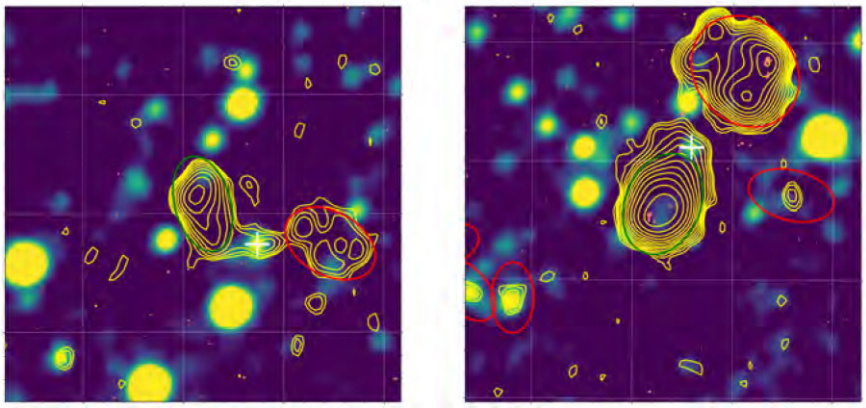

**Figure 9.** Example postage stamps of radio sources in the G23 field. ASKAP contours (yellow) and VLASS contours (salmon) on *WISE* images (colour). Each postage stamp is centred at the position of the source component to be inspected (indicated by a green ellipse). The red ellipse shows the neighbouring source and the white cross indicates the host galaxy position. ASKAP and VLASS contours denote the surface brightness levels starting at $3\sigma$ and increasing at various powers of $3\sigma$ (off-source rms noise).

**Table 5.** The source statistics based on the modified envelope (see Section 3.3) and the final catalogue.

| Source type | Count |
|---|---|
| Total unresolved sources | 32 637 |
| Total resolved sources | 7175 |
| Visually identified sources with 1 component | 175 |
| Visually identified sources with 2 components | 86 |
| Visually identified sources with ≥3 components | 44 |

**Table 6.** 887.5 MHz source counts as derived from our survey. *Column 1:* flux interval ($\Delta S$); *Column 2:* geometric mean of the flux density ($\langle S \rangle$); *Column 3:* number of sources detected ($N_S$); *Column 4:* differential counts normalized to a non-evolving Euclidean model ($n\ S^{2.5}$); *Columns 5 and 6:* Poissonian errors on the normalized counts.

| $\Delta S$ (mJy) | $\langle S \rangle$ (mJy) | $N_S$ | $dN/dS\ S^{2.5}$ ($sr^{-1}\ Jy^{1.5}$) | $\sigma^-$ | $\sigma^+$ |
|---|---|---|---|---|---|
| 0.20–0.29 | 0.24 | 7513 | 7.48 | 0.09 | 0.09 |
| 0.29–0.41 | 0.34 | 8426 | 8.63 | 0.09 | 0.10 |
| 0.41–0.57 | 0.48 | 6148 | 9.01 | 0.11 | 0.12 |
| 0.57–0.81 | 0.68 | 4195 | 9.42 | 0.15 | 0.15 |
| 0.81–1.15 | 0.97 | 2732 | 9.77 | 0.19 | 0.19 |
| 1.15–1.63 | 1.37 | 1971 | 11.61 | 0.26 | 0.27 |
| 1.63–2.30 | 1.94 | 1334 | 13.10 | 0.36 | 0.37 |
| 2.30–3.25 | 2.74 | 1020 | 16.77 | 0.53 | 0.54 |
| 3.25–4.60 | 3.87 | 835 | 23.04 | 0.80 | 0.82 |
| 4.60–6.51 | 5.47 | 660 | 30.5 | 1.2 | 1.2 |
| 6.51–9.20 | 7.74 | 551 | 42.9 | 1.8 | 1.9 |
| 9.20–13.0 | 10.9 | 417 | 54.5 | 2.7 | 2.8 |
| 13.0–26.0 | 18.4 | 627 | 88.1 | 3.5 | 3.7 |
| 26.0–52.1 | 36.8 | 417 | 165.5 | 8.1 | 8.5 |
| 52.1–104 | 73.6 | 213 | 239 | 16 | 17 |
| 104–417 | 208 | 149 | 375 | 31 | 33 |
| 417–1666 | 833 | 25 | 504 | 101 | 121 |

utilized the multiwavelength catalogue described above. Since the multiwavelength catalogue takes GAMA sources as its base, there are GAMA sources with or without *WISE* counterparts. In the process of host galaxy identification, if a radio source has a GAMA counterpart we take this as the host, and if not we take the *WISE* counterpart as the host.

Sources classified as 'single' (S_Code = S) in the catalogue were initially cross-matched with the multiwavelength catalogue assuming a matching distance of up to 2 arcsec. This value was chosen by estimating the incidence of false cross-identifications as a function of matching distance. We generated a mock catalogue of optical sources with random positions and cross-matched this mock catalogue with the radio source catalogue for a range of matching radii. We estimated the fraction of matches as a function of matching radius. Above a match radius of about 2 arcsec, the number of matches stays approximately unchanged for any further increase in separation distance, and this is taken as the best pairing distance estimate. At 2 arcsec separation, the predicted contamination ($N_{random}/N_{true}$, where $N_{true}$ is estimated by subtracting the total random matches from the corresponding value for the real catalogue) in the overall sample is around 7 per cent. Naturally, a larger matching radius would lead to a higher number of identifications and consequently to a more complete catalogue with identifications. At this adopted separation, the completeness rate (given by the fraction of true matches out of all matches) is around 85 per cent.

The majority of the remaining sources were then visually inspected using the postage stamps (see 9) that show ASKAP and VLASS contours on *WISE* images in order to identify and collect objects with multiple components (two examples of the postage stamps are shown in Fig. 9). The selected possible multicomponent radio sources were run through another visual inspection utilizing a tool, which displays the radio data as well as overlaying a catalogue of optical (GAMA) or IR (*WISE*) sources around the target source to be classified. This process involved associating individually detected ASKAP sources, identifying any remaining artefacts, and, for real sources, specifying any plausible optical identification for the radio source. Here, VLASS images had an important role, as they often show the flat-spectrum core of an extended ASKAP source making optical identification far more robust.

We provide source sizes in the final catalogue along with source flux densities (in the case of multicomponent sources, a sum of component flux densities was stored), following a similar method presented by Williams et al. (2019). We first determined the convex hull around the set of elliptical Gaussians: the convex hull is the smallest convex shape that contains all of the ellipses. We constructed the convex hull of multicomponent sources by representing each component (PyBDSF source or PyBDSF Gaussian as appropriate) as an ellipse, where the deconvolved FWHM major and minor axes

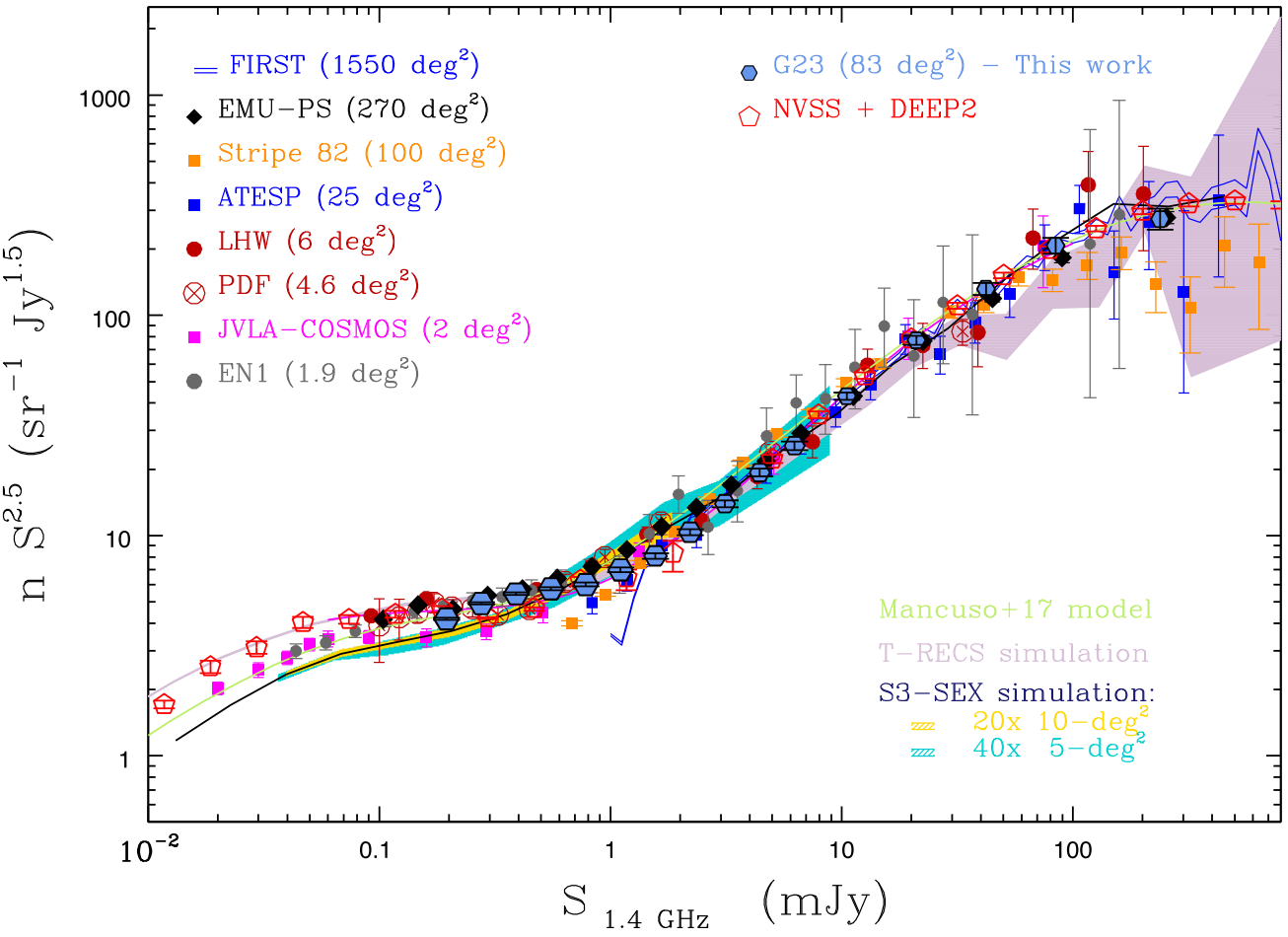


**Figure 10.** Normalized differential source counts derived from the G23 radio source catalogue (blue hexagons bordered in black). The counts have been rescaled from 887.5 MHz to 1.4 GHz by assuming $\alpha = 0.7$. Vertical bars represent Poissonian errors on the normalized counts (computed following Regener 1951). Systematic errors due to incompleteness and bias corrections, as well as spectral index assumptions, scale with the size of the plotted symbols. Also shown for comparison are the counts derived from other wide-field ($\gg$1 deg$^2$) surveys. All the surveys shown in this plot are taken at frequencies at or near 1.4 GHz, to minimize systematic errors introduced when rescaling the counts to 1.4 GHz. Unless stated differently, the rescaling has been done by assuming $\alpha = 0.7$, as for the G23 survey. The surveys are listed in the legend: these are the FIRST survey (White et al. 1997), the 943.5 MHz EMU Pilot Survey (EMU-PS; Norris et al. 2021), the SDSS STRIPE-82 mosaic (Heywood et al. 2016), the ATESP survey (Prandoni et al. 2001), the Westerbork Lockman Hole mosaic (LHW; Prandoni et al. 2018), the Phoenix Deep Survey (PDF; Hopkins et al. 2003), the 3 GHz JVLA-COSMOS project (rescaled to 1.4 GHz by Smolčić et al. 2017a, by exploiting measured source spectral indices, whenever available), and the 610 MHz survey of the ELAIS-N1 (EN1) field (Ocran et al. 2020). Also shown are the recent counts obtained by Matthews et al. (2021) by combining the NVSS and the MeerKAT DEEP2 field (1 deg$^2$), which span eight decades of flux density. The yellow and light blue shaded areas illustrate the predicted cosmic variance effects for survey coverages of 5 and 10 deg$^2$, respectively. They have been obtained by splitting the S3-SEX simulation of Wilman et al. (2008) (covering $1 \times 200$ deg$^2$; see black line) into 40 5-deg$^2$ and 20 10-deg$^2$ fields, respectively. The 25 deg$^2$ medium tier of the more recent T-RECS simulations (Bonaldi et al. 2019) is represented by the violet shaded area. Finally, the counts derived from the Mancuso et al. (2017) radio source evolutionary model are indicated by the light green solid line.

are taken to be, respectively, the semimajor and semiminor axes of the ellipse. The convex hull was constructed around all of the component ellipses using the SHAPELY PYTHON package. The length of the largest diameter of the convex hull around the set of elliptical Gaussians (i.e. the maximum angular separation where all points on the convex hull considered pairwise) would give an estimate of a source size ('Length'). Sizes based on this presented method are likely to overestimate the true size in general. Another approach would be estimating the separation between the farthest components (e.g. Hardcastle et al. 2016) but this will underestimate the true size (given as 'Separation' column in the catalogue). For this reason, we took the mean value of the length of the largest diameter of the convex hull around the set of elliptical Gaussians (i.e. Length) and the distance between the most separated components ('Separation') of a source as our true sizes ('Size'). The source position angle (given as 'PA' column) was taken to be the position angle on the sky of that largest diameter vector. For the source width ('Width'), we adopted twice the maximum perpendicular distance of points on the convex hull to the largest diameter vector. For the sources classified as 'single', we provided the major ('Maj'), minor ('Min'), and deconvolved major ('DC_Maj') and minor axes ('DC_Min') of the Gaussian along with the errors on these measurements provided by PyBDSF, and its position angle. The error measurements do not take into account systematic effects (i.e. smearing that is expected to reduce peak fluxes by at most 2 per cent and ionosphere; see Section 3.3) that would affect the source size. This amount can

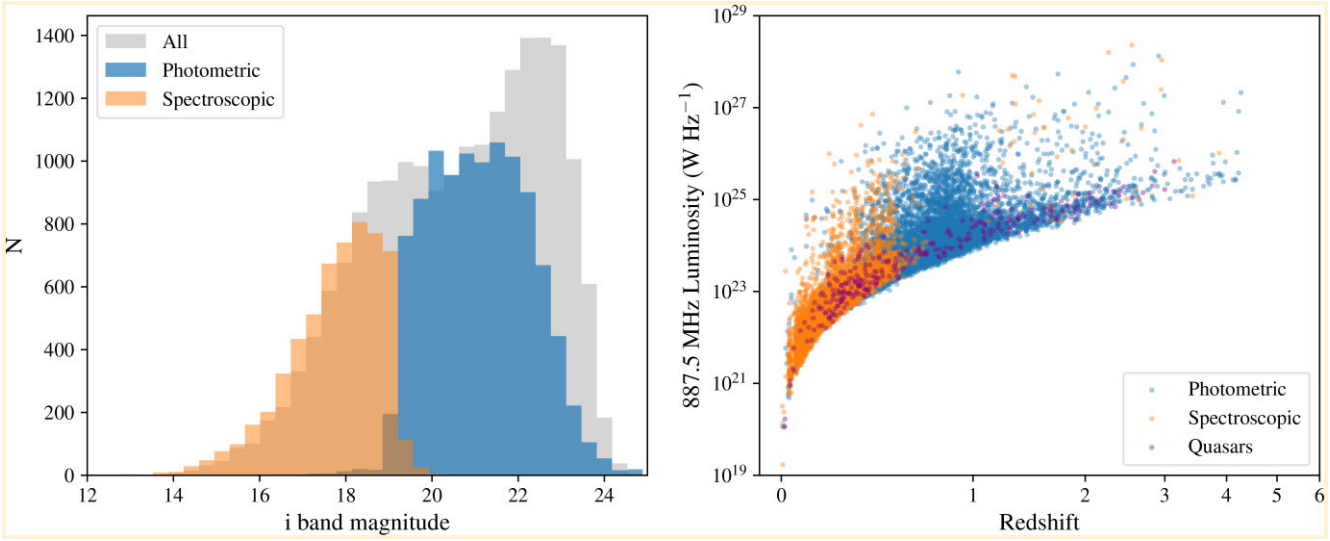


**Figure 11.** Left: *i*-band magnitude distribution of identified sources with spectroscopic redshifts, photometric redshifts, and all galaxies. Right: Radio luminosity distribution of sources with photometric redshifts, spectroscopic redshifts, and quasars as a function of source redshift. Redshift is plotted on a log $(1 + z)$ scale but labelled with $z$ values.

**Table 7.** Number of sources with spectroscopic redshifts (spec-$z$) and photometric redshifts (photo-$z$). We also present the number of sources with reliable (see Section 4.1) photometric redshifts.

| Source class | Count |
|---|---|
| Sources with GAMA counterpart | 20 007 |
| Sources with *WISE* counterpart | 5080 |
| Sources with spec-$z$ | 5934 |
| Sources with photo-$z$ | 14 776 |
| Sources with reliable photo-$z$ | 11 583 |

**Table 8.** The number of sources in each population after the optical emission-line classification and the median spectroscopic redshift for each population.

| Emission line class | Count | Median redshift |
|---|---|---|
| SFGs | 1636 | 0.163 |
| Composites | 384 | 0.18 |
| AGNs | 261 | 0.213 |
| LINERs | 13 | 0.178 |
| Unclassified | 4022 | 0.227 |

be added in quadrature to the given errors. The estimation of the error in source size is less straightforward for extended radio sources (i.e. multicomponent objects). The relative error on sources with deconvolved sizes larger than 20 arcsec (and detected at $10\sigma$) is around 10 per cent and this is much lower for larger size objects. Based on this, we can safely suggest that sources with multiple components should have relative errors smaller than this value. It is worth noting that estimating both sizes and size errors is even more complicated for radio sources with bent morphology. The final catalogue has 39 812 sources detected at $5\sigma$ and 25 087 (63 per cent based on the matching radius we use) objects have host galaxy counterparts (either GAMA or *WISE*). The numbers of unresolved sources, resolved sources, and sources with multiple components are given in Table 5.

### 4.3 Source counts

The differential source counts obtained from the G23 source catalogue, normalized to a non-evolving Euclidean model ($S^{2.5}$), are listed in Table 6 and shown in Fig. 10 (black-bordered blue hexagons). The source counts are corrected for both Eddington bias (Eddington 1913, 1940) and resolution bias (i.e. the fact that a larger source of a given total flux density will drop below the signal-to-noise threshold of a survey more easily than a smaller source of the same total flux density). This is done following standard recipes in the literature (see e.g. Prandoni et al. 2001, 2018; Mandal et al. 2021). The counts are also corrected for catalogue incompleteness and spurious detections, based on the results of the simulations presented in Section 3.3.

Fig. 10 compares the G23 source counts (rescaled from 887.5 MHz to 1.4 GHz by assuming $\alpha = 0.7$) with counts derived from some of the widest area samples available to date at 1.4 GHz. This includes sub-mJy surveys covering >1 deg$^2$ regions, like the Phoenix Deep Field (PDF; 4.6 deg$^2$; Hopkins et al. 2003) and the Westerbork 6 deg$^2$ mosaic covering the Lockman Hole (LH) region (LHW; Prandoni et al. 2018), as well as shallower (>1 mJy) but larger (>>10 sq. deg) surveys like ATESP (25 deg$^2$; Prandoni et al. 2001), Sloan Digital Sky Survey (SDSS) Stripe 82 (100 deg$^2$; Heywood et al. 2016), FIRST (1550 deg$^2$; White et al. 1997), and the very recent determination obtained by combining NVSS and confusion-limited MeerKAT L-band observations of the DEEP2 field (1 deg$^2$; Matthews et al. 2021). Also shown are counts derived from wide-area sub-mJy surveys taken at similar frequencies to G23: namely the ELAIS-N1 field observed at 610 MHz (EN1, 1.9 deg$^2$; Ocran et al. 2020) and the EMU Pilot Survey (EMU-PS, 270 deg$^2$; Norris et al. 2021), taken at 943.5 MHz. Furthermore, we show the deep counts obtained from the 3 GHz JVLA-COSMOS project (2 deg$^2$; Smolčić et al. 2017a). All such counts are rescaled to 1.4 GHz assuming the same spectral index as for G23, except for the JVLA-COSMOS project, where measured spectral indices were available for a fraction of the sources. Finally, we show 1.4 GHz simulated source counts derived from the source evolutionary model of Mancuso et al. (2017, light green solid line), from the T-RECS 25 deg$^2$ medium tier simulation (Bonaldi et al. 2019, violet shaded area), as well as different realizations obtained from the S3-SEX simulated catalogue (Wilman et al. 2008):

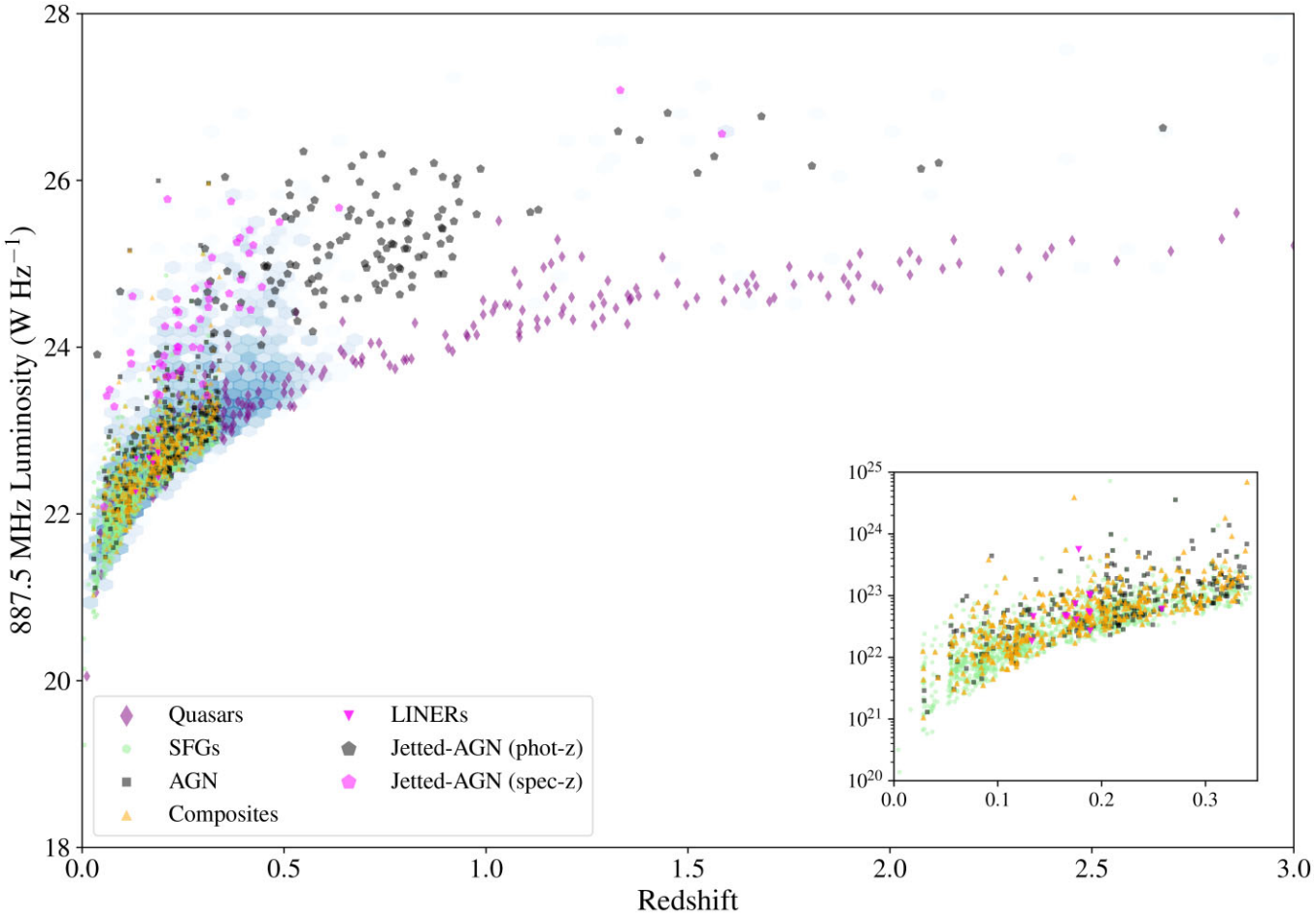


**Figure 12.** Combined density/scatter figure showing the distribution of the luminosity at 887.5 MHz of all ASKAP-detected galaxies in the sample as a function of their redshifts. Colours and different symbols indicate different emission-line classes. Blue hexagons show the density of sources unclassified by their optical emission lines. Other sources are shown with a symbol for each object: these include SFGs (light green circles), composites (orange triangle point up), AGNs (black squares), and LINERs (pink triangle point down) and jetted AGNs (pentagons: magenta with spectroscopic redshift and grey with photometric redshift). Quasars are shown as purple diamonds. The inner panel shows only sources classified by the optical emission lines using the same symbols.

$1 \times 200$ deg$^2$ (black solid line), $20 \times 10$ deg$^2$ regions (light blue shaded area), and $40 \times 5$ deg$^2$ regions (yellow shaded area).

Fig. 10 clearly demonstrates that the source counts derived from the G23 catalogue nicely match previous counts derived from wide-area surveys, and are in good agreement with the most recent simulations (Bonaldi et al. 2019), at the same time providing very robust statistics over the entire flux range spanned by the source catalogue. It is noteworthy that there is a quite good agreement with the recent EMU-PS counts (Norris et al. 2021), also obtained with ASKAP, and with Matthews et al. (2021) counts, which are the most robust to date, down to 10 μJy.

### 4.4 Source properties

There are in total 25 087 sources with host galaxy counterparts. Out of the 323 multicomponent radio sources (identified and combined via visual inspection), 264 have a host galaxy identification, and 56 of these latter have spectroscopic redshifts and 130 have reliable photometric redshifts. We also cross-matched our final catalogue with the latest release of the MilliQuas catalogue that contains quasars and quasar candidates (v7.2; Flesch 2021) within 2 arcsec (here, we used the coordinates of the radio sources), which provided 591 matches. In the rest of the work, we only show sources that are classified as quasars (i.e. the type column equals to Q or q) from this catalogue. In the left-hand panel of Fig. 11, we show the apparent *i*-band magnitude distribution of sources identified with spectroscopic, photometric, and no redshifts. We see that the our radio source sample is virtually spectroscopically complete up to around $i \sim 18$ and becomes severely incomplete at $i > 18.8$. The numbers of sources with either spectroscopic or photometric redshifts are given in Table 7.

In the right-hand panel of the same figure (Fig. 11), we show the distribution of rest-frame radio luminosity at 887.5 MHz (using a spectral index of 0.7) as a function of source redshift. In this panel, we also show sources that have matches in the MilliQuas-V7.2 catalogue (we use our redshifts where available; otherwise, we use redshifts published in the MilliQuas v7.2 catalogue for quasars). Similarly, it can be seen that the majority of spectroscopic redshifts are limited to $z \sim 0.6$. The highest redshift object in the sample is a quasar at $z = 6.44$ (Decarli et al. 2018). Here, we provide a more reliable estimate of this high-redshift source using our carefully imaged data. The total flux density of this quasar at 887.5 MHz is $0.68 \pm 0.065$ mJy [as opposed to the reported value $0.59 \pm 0.07$ mJy by Ighina et al. (2021) using the old ASKAP mosaic of G23] and for a redshift of 6.44 the rest-frame radio luminosity of the quasar corresponds to $1.84 \times 10^{26}$ W Hz$^{-1}$.

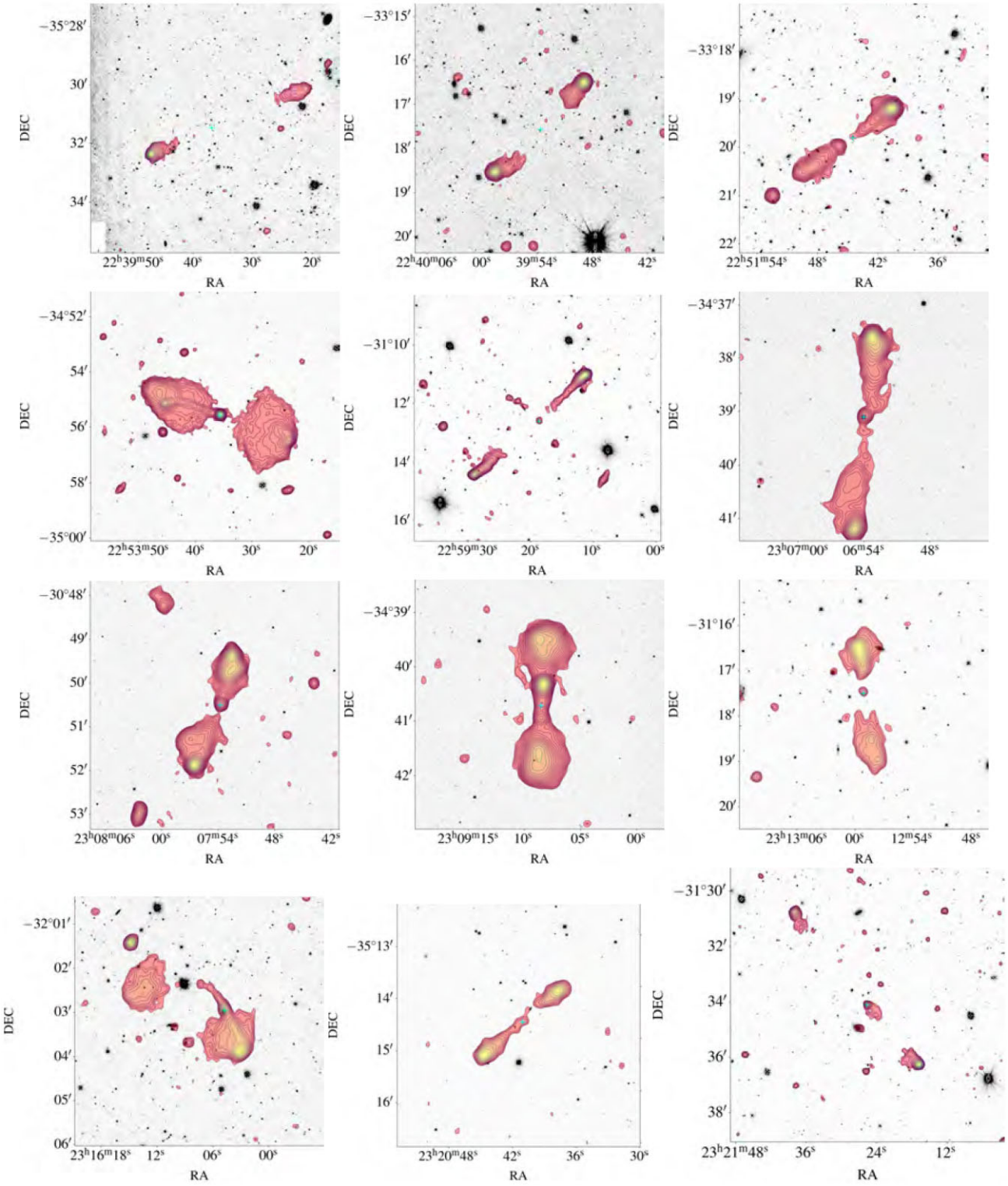


**Figure 13.** Example of GRGs newly discovered as part of the ASKAP observations in the G23 field. Background images are from KiDS. Salmon colour density maps show the ASKAP data. Cyan crosses show host galaxy positions. Density contours denote the surface brightness levels starting at $3\sigma$ and increasing at various powers of $3\sigma$, where $\sigma$ denotes the local RMS noise in each map.

We further classify our sources by their optical emission lines available to us (Gordon et al. 2017). For this, we use Baldwin–Phillips–Terlevich-type (Baldwin, Phillips & Terlevich 1981) emission-line diagnostics described by Kewley et al. (2006). Our classification was carried out using only the following emission lines: [N II] λ6583, [S II] λ6717, H $\beta$, O III λ5007, and H $\alpha$. Before implementing our selection, we also corrected the flux of H $\alpha$ and H $\beta$ lines for stellar absorption (Gordon et al. 2017). Composite

objects were separated from SFGs using the criterion given by Kauffmann et al. (2003). It is necessary for objects to have the required optical emission lines – in our case H $\beta$, O III $\lambda$5007, H $\alpha$, [N II] $\lambda$6583, and [S II] $\lambda$6717 – detected at $3\sigma$ in order to classify galaxies accurately. The number of sources in each population after optical emission-line classification is given in Table 8. The rest-frame radio luminosity distribution of sources classified based on the optical emission lines as a function of redshift is seen (Fig. 12). A large number of galaxies, more than half the parent sample, are not detected in all the required optical emission lines at $3\sigma$, and those are therefore unclassified by the methods we use. These are shown in Fig. 12 as blue density plots. As discussed by Gürkan et al. (2018), a fraction of these sources are a contaminating population of low-luminosity AGNs whereas some might be high-redshift SFGs. The optically selected sample (AGNs: black squares, SFGs: light green circles, Composites: orange triangle point up, and LINERs: pink triangle point down) shows similar radio luminosities as can be seen in the inner panel of Fig. 12 except that some AGNs have quite high radio luminosity. We also show radio sources having components resolved in our map using pentagon symbols (magenta for objects with spectroscopic redshift and grey for sources with photometric redshift). As expected, these sources have much higher radio luminosities than sources selected by their optical emission lines. Quasars (i.e. matches in the MilliQuas-V7.2 catalogue) are shown as purple diamonds. It is not surprising that quasars have the widest redshift coverage and a fraction of these objects present high radio luminosities.

### 4.5 Giant radio galaxies

In AGNs, the energy is generated by accretion of matter on to SMBHs in the centre of active galaxies. This accretion can give rise to relativistic jets, which are mainly observed at radio wavelengths. These AGN-driven relativistic jets can have a range of sizes; at typical distances, the largest angular scales can reach to several arcminutes, which might be corresponding to hundreds of kpc. GRGs have the largest projected linear sizes up to $\sim$5 Mpc (Willis, Strom & Wilson 1974; Ishwara-Chandra & Saikia 1999). Dabhade et al. (2020) recently released the largest sample of GRGs identified in a radio survey using data from LoTSS. It is still debated how a fraction of jetted AGNs acquire such gigantic sizes. Among the suggested reasons for their large sizes, there are a few possibilities considered such as GRGs reside in sparser environments (e.g. Saripalli & Malarecki 2015; Dabhade et al. 2020), allowing them to grow fast and reach to larger distances (but see Lan & Prochaska 2021), or GRGs are the result of recurrent radio jet activity (Bruni et al. 2020). Furthermore, they appear to have different central engine properties (Hardcastle et al. 2019) and lifetime distributions (Shabala et al. 2020) compared to standard jetted AGNs.

ASKAP's excellent capability of rapidly observing wide fields, providing radio data at high sensitivities and resolution in conjunction with the multiwavelength data available for the G23 field, allowed us to discover several GRGs, some of which are shown in Fig. 13. These include the well-known GRG studied in detail by (the bottom right one in Fig. 13) Seymour et al. (2020). Following the literature, we classify a source to be a GRG if its size $>$0.7 Mpc. There are 63 sources (among sources with reliable spectroscopic and photometric redshifts) meeting this criterion. As a sanity check, it is interesting to see where our GRGs fall in the so-called *P–D* diagram (i.e. the plane identified by radio power and source linear size of jetted AGNs; Baldwin 1982; Hardcastle 2018; Turner et al. 2018; Hardcastle et al. 2019). In order to make a comparison to other AGN samples like the 3CRR sample of Laing, Riley & Longair (1983) and the one constructed using the LoTSS data (Hardcastle et al. 2019), we extrapolated the radio luminosity of our AGN sample from 887.5 to 150 MHz using a radio spectral index of 0.7. The *P–D* diagram is shown in Fig. 14. Different AGN classes are shown with different symbols (see the figure legend).

We also show the theoretical tracks first introduced by Hardcastle (2018) for $z = 0$ sources lying in the plane of the sky in a group environment ($M_{500}$[6] $= 2.5 \times 10^{13}$ M$_\odot$, $kT = 1$ keV) for two-sided jet powers (from bottom to top) $Q = 10^{35}, 10^{36}, ..., 10^{40}$ W. The *P–D* diagram has been traditionally used to understand the evolutionary path of jetted AGNs. Although it is not straightforward to infer direct information about AGNs based on their location in the *P–D* diagram (due to various effects such as radio galaxy environment, Doppler boosting, and the source angle to the line of sight), it is still invaluable for interpreting the evolution of AGN populations and GRGs. The theoretical tracks are derived from a model that predicts the time evolution of both luminosity and physical size in a given environment and for a given jet power $Q$ (defined as the two-sided power, i.e. the total kinetic power of both jets; for further details, we refer the reader to Hardcastle et al. 2019). The positions of the time evolution markers on the tracks show that, if all jetted AGNs have long lifetimes, we expect them to spend most of their lifetime with (unprojected) sizes between a few tens and a few hundreds of kpc.

In Fig. 14, we show resolved AGNs that were identified by visual inspection (with clearly resolved components) as well as sources with sizes larger than 35 arcsec (this is because showing only sources identified by visual inspection will miss jetted AGNs whose components were combined by the source finder algorithm), quasars and GRGs. If we evaluate our sources displayed in the *P–D* diagram based on only the normalization of the tracks, we see that the majority of jetted AGNs, radio sources with large linear sizes (i.e. size $>$35 arcsec), and quasars in these models correspond to a jet power $\gtrsim 10^{35}$ W similar to LoTSS AGNs, though there is a considerable number of quasars that have jet powers lower than $10^{35}$ W (occupying the region where we see LoTSS AGNs with size limits). The overabundance of these compact sources reinforces the idea that many more short-lived sources occur compared to long-lived ones (i.e. the fact that the *P–D* distribution shows that most sources do *not* have sizes of 10s–100s kpc), as suggested by Shabala et al. (2020) and Hardcastle et al. (2019), though it should be noted that the radio emission from some of these quasars might be dominated by star formation (e.g. Gürkan et al. 2019; Macfarlane et al. 2021). Finally, GRGs that we discovered in our survey occupy the tail in these models and correspond to similar jet powers with extensive sizes ($P > 10^{38}$ W, size $>$700 kpc) where we expect jetted AGNs to spend most of their lifetime.

## 5 CONCLUSIONS AND FUTURE PROSPECTS

We have presented ASKAP observations of the G23 field made as part of the EMU Early Science programme. The imaging data products presented as part of this study form the first wide-area (82.7 deg$^2$), high-resolution (10 arcsec) and high-sensitivity (with a central rms off-source noise of 38 $\mu$Jy beam$^{-1}$) survey of the G23 field carried out at 887.5 MHz using ASKAP. We have quantified the positional and flux density accuracy of the ASKAP sources in the field. We have presented the differential source counts at 887.5 MHz,

[6]Here, $M_{500}$ stands for the total mass of the system within the radius $R_{500}$, and $kT$ indicates the temperature of X-ray-emitting gas of the galaxy group.

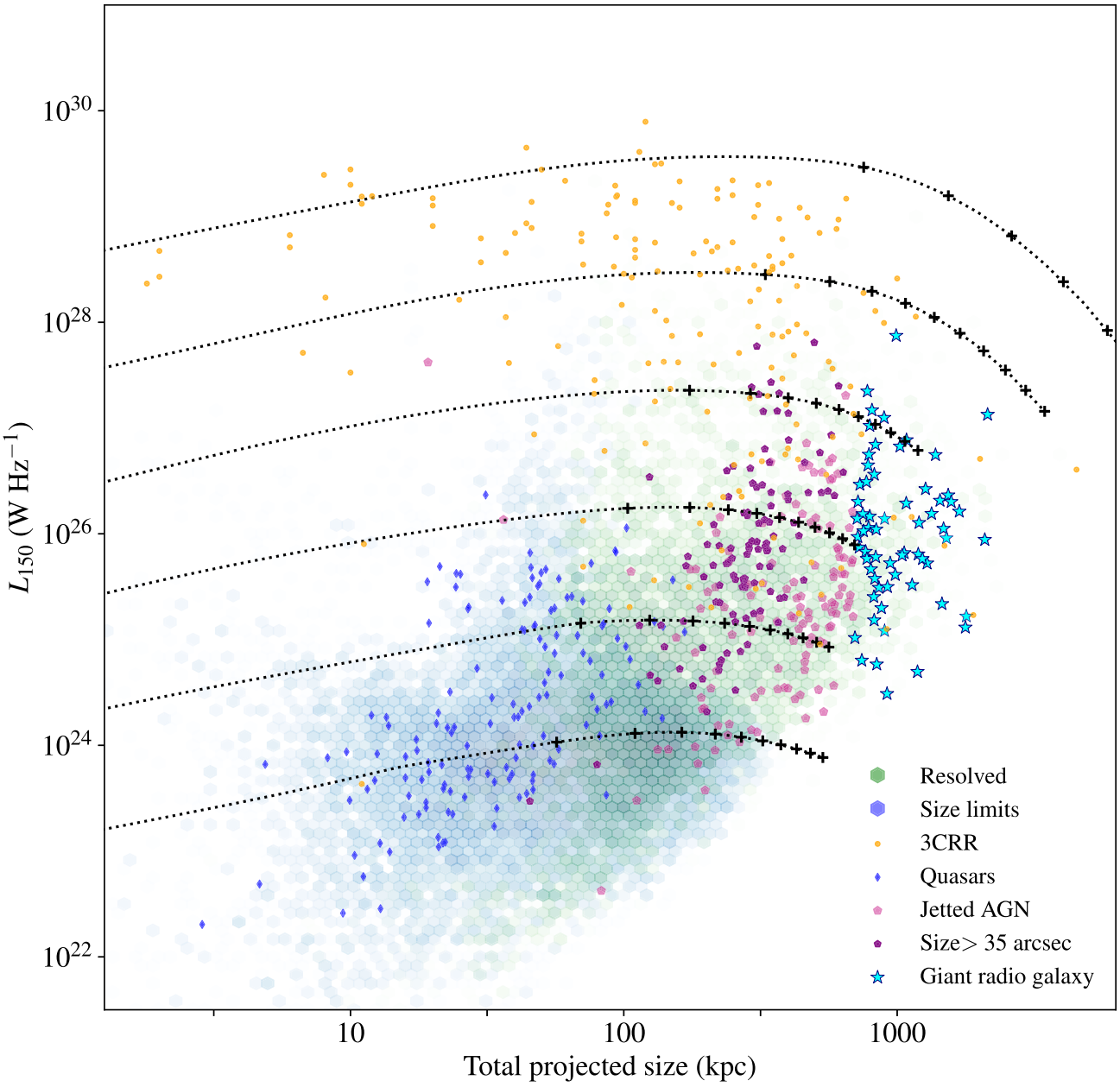


**Figure 14.** Radio power–linear size (*P–D* diagram) for the AGN sample. Blue and green density hexagons show unresolved and resolved LoTSS jetted-AGN samples (Hardcastle et al. 2019). Pink circles are 3CRR sources from Laing et al. (1983). Quasars found in our survey by matching our final catalogue with the MilliQuas v7.2 catalogue (Flesch 2021) are shown as blue diamonds. Radio sources with resolved multiple components that were identified through visual inspection are seen as purple pentagons, whereas radio sources with sizes larger than 35 arcsec are shown as pink pentagons. Cyan stars indicate GRGs. We also show the theoretical evolutionary tracks published by Hardcastle et al. (2019) for $z = 0$ sources lying in the plane of the sky in a group environment ($M_{500}$ = 2.5 × $10^{13}$ $M_{\odot}$, $kT$ = 1 keV) for two-sided jet powers (from bottom to top) $Q = 10^{35}$, $10^{36}$, ..., $10^{40}$ W. Crosses on the tracks are plotted at intervals of 50 Myr, where linear size increases monotonically with time; each track lasts for 500 Myr in total. Here, the ASKAP radio luminosities of sources at 887.5 MHz were extrapolated to 150 MHz using a spectral index of 0.7.

which follow quite well the model predictions of various studies and several radio counts that were published previously using other radio surveys. The outcome of our efforts to combine all physically associated radio sources into single objects (Section 4.2) along with their properties (their correct flux densities and sizes) is one of the major products of this paper. Using the multiwavelength photometric and optical spectroscopic catalogues, we identified host galaxy counterparts of the majority of radio sources in the final catalogue (around 63 per cent). The synergy between excellent ASKAP data and multiwavelength catalogues allowed us to discover new GRGs in the field (63 in total).

Subsequent papers will investigate various source classifications and revisit the evaluation of photometric redshifts (Marchetti et al. in prep.), explore the link between radio luminosity and AGN outflows for low-luminosity sources (Prandoni et al., in preparation), and further investigate the GRGs (Gürkan et al., in preparation). The data

**Table 9.** The FITS catalogue columns and their descriptions.

| Column name (unit) | Description |
|---|---|
| Source name | Source name that is generated using the final radio source position |
| RA (deg) and E RA (deg) | Flux-weighted right ascension (RA) and uncertainty |
| Dec. (deg) and E Dec. (deg) | Flux-weighted declination (Dec.) and uncertainty |
| Total flux (Jy) and E Total Flux (Jy) | Integrated source flux density and uncertainty |
| Peak flux (Jy beam$^{-1}$) and E Peak Flux (Jy beam$^{-1}$) | Peak flux density and uncertainty |
| Length (arcsec) | Source length |
| Width (arcsec) | Source width |
| PA (deg) | Position angle |
| DC Maj (arcsec) and E DC Maj (arcsec) | Deconvolved major axis and uncertainty |
| DC Min (arcsec) and E DC Min (arcsec) | Deconvolved minor axis and uncertainty |
| Maj (arcsec) and E Maj (arcsec) | Major axis and uncertainty |
| Min (arcsec) and E Min (arcsec) | Minor axis and uncertainty |
| Separation (arcsec) | Separation between the farthest components |
| Isl rms (Jy beam$^{-1}$) | The local rms noise used for the source detection |
| SCode | Source morphology code; M indicates sources with multiple components that were identified via visual inspection |
| Size (arcsec) | Source size (the size of multicomponent radio sources is estimated as the average of length and separation and deconvolved major axis is used for the rest) |

products presented here are expected to be reasonably representative in data quality of the much larger EMU survey currently being carried out. Value-added information constructed as part of this work and its quality (as shown here) as well as the preliminary results from ongoing studies demonstrate excellent capabilities of ASKAP in terms of observing wide fields swiftly, its data quality, and the scientific use of its data, which will contribute to the first steps towards the exciting science with ASKAP in the pre-SKA era.

## ACKNOWLEDGEMENTS

We thank the anonymous referee for their constructive comments. We thank Aaron Chippendale for assisting us to produce Fig. 1, Daniel Mitchell and Mark Wieringa for their discussion with respect to the mosaicking function, and Martin Hardcastle for making the data available to replicate Fig. 8 in their work. IP acknowledges support from Istituto Nazionale di Astrofisica (INAF) under the SKA/CTA PRIN 'FORECaST' and the PRIN MAIN STREAM 'SAuROS' projects and from CSIRO under its Distinguished Research Visitor Programme. LM, IP, and MV acknowledge support from the Italian Ministry of Foreign Affairs and International Cooperation (MAECI grant number ZA18GR02) and the South African Department of Science and Innovation's National Research Foundation (DSI-NRF grant number 113121) under the ISARP RADIOSKY2020 Joint Research Scheme. DL is supported by a grant from the Natural Sciences and Engineering Research Council of Canada. MB is supported by the Polish National Science Centre through grant numbers 2020/38/E/ST9/00395, 2018/30/E/ST9/00698, and 2018/31/G/ST9/03388, and by the Polish Ministry of Science and Higher Education through grant DIR/WK/2018/12. This paper includes archived data obtained through the Commonwealth Scientific and Industrial Research Organisation (CSIRO) Australian Square Kilometre Array Pathfinder (ASKAP) Science Data Archive (CASDA; http://data.csiro.au). The ASKAP is part of the Australia Telescope National Facility (grid.421683.a) that is managed by CSIRO. Operation of ASKAP is funded by the Australian Government with support from the National Collaborative Research Infrastructure Strategy. ASKAP uses the resources of the Pawsey Supercomputing Centre. Establishment of ASKAP, the Murchison Radio-astronomy Observatory (MRO), and the Pawsey Supercomputing Centre are initiatives of the Australian Government, with support from the Government of Western Australia and the Science and Industry Endowment Fund. We acknowledge the Wajarri Yamatji people as the traditional owners of the observatory site. We acknowledge the use of the Ilifu cloud computing facility, http://www.ilifu.ac.za, a partnership between the University of Cape Town, the University of the Western Cape, the University of Stellenbosch, Sol Plaatje University, the Cape Peninsula University of Technology, and the South African Radio Astronomy Observatory. The Ilifu facility is supported by contributions from the Inter-University Institute for Data Intensive Astronomy (IDIA – a partnership between the University of Cape Town, the University of Pretoria, the University of the Western Cape, and the South African Radio astronomy Observatory), the Computational Biology division at UCT, and the Data Intensive Research Initiative of South Africa (DIRISA). This research has made use of the University of Hertfordshire high-performance computing facility (http://uhhpc.herts.ac.uk/) located at the University of Hertfordshire. This research made use of astropy, a community-developed core PYTHON package for astronomy (Aceituno et al. 2013) hosted at http://www.astropy.org/, and of TOPCAT (Taylor 2005). This research has made use of the CIRADA cutout service at cutouts.cirada.ca, operated by the Canadian Initiative for Radio Astronomy Data Analysis (CIRADA). CIRADA is funded by a grant from the Canada Foundation for Innovation 2017 Innovation Fund (Project 35999), as well as by the Provinces of Ontario, British Columbia, Alberta, Manitoba, and Quebec, in collaboration with the National Research Council of Canada, the US National Radio Astronomy Observatory, and Australia's CSIRO.

## DATA AVAILABILITY

The data underlying this article are available in the article and in its online supplementary material. Calibrated visibilities of the data (scheduling blocks 8132 and 8137) used for this work are available on the CSIRO ASKAP Science Data Archive (CASDA). The final radio source catalogue produced as a result of our analysis and visual inspection (Section 4.2) is made available for download in FITS

format as part of the supplementary material. Table 9 below gives the column names and descriptions.

## REFERENCES


Aceituno J. et al., 2013, A&A, 552, A31
Allison J. R., Zwaan M. A., Duchesne S. W., Curran S. J., 2016, MNRAS, 462, 1341
Allison J. R. et al., 2020, MNRAS, 494, 3627
Baldry I. K. et al., 2012, MNRAS, 421, 621
Baldwin J. E., 1982, in Heeschen D. S., Wade C. M., eds, Proc. IAU Symp. 97, Extragalactic Radio Sources. Kluwer, Dordrecht, p. 21
Baldwin J. A., Phillips M. M., Terlevich R., 1981, PASP, 93, 5
Becker R. H., White R. L., Helfand D. J., 1995, ApJ, 450, 559
Bellstedt S. et al., 2020, MNRAS, 496, 3235
Best P. N., Ker L. M., Simpson C., Rigby E. E., Sabater J., 2014, MNRAS, 445, 955
Blundell K. M., Rawlings S., 2000, AJ, 119, 1111
Boggs P. T., Rogers J. E., 1990, Contemp. Math., 112, 186
Bonaldi A., Bonato M., Galluzzi V., Harrison I., Massardi M., Kay S., De Zotti G., Brown M. L., 2019, MNRAS, 482, 2
Bourne N. et al., 2016, MNRAS, 462, 1714
Brammer G. B., van Dokkum P. G., Coppi P., 2008, ApJ, 686, 1503
Brown M. J. I. et al., 2014, ApJS, 212, 18
Bruni G. et al., 2020, MNRAS, 494, 902
Brunner H. et al., 2021, preprint (arXiv:2106.14517)
Condon J. J., 1992, ARA&A, 30, 575
Condon J. J., 1997, PASP, 109, 166
Condon J., 2015, preprint (arXiv:1502.05616)
Condon J. J. , Cotton W. D., Greisen E. W., Yin Q. F., Perley R. A., Taylor G. B., Broderick J. J., 1998, AJ, 115, 1693
Dabhade P. et al., 2020, A&A, 635, A5
de Gasperin F. et al., 2021, A&A, 648, A104
de Jong J. T. A., Verdoes Kleijn G. A., Kuijken K. H., Valentijn E. A., 2013, Exp. Astron., 35, 25
de Jong J. T. A. et al., 2015, A&A, 582, A62
Decarli R. et al., 2018, ApJ, 854, 97
Driver S. P. et al., 2011, MNRAS, 413, 971
Driver S. P. et al., 2016, MNRAS, 455, 3911
Driver S. P. et al., 2022, MNRAS, in press
Duncan K. J. et al., 2018a, MNRAS, 473, 2655
Duncan K. J., Jarvis M. J., Brown M. J. I., Röttgering H. J. A., 2018b, MNRAS, 477, 5177
Eddington A. S. S., 1940, MNRAS, 100, 354
Eddington A. S., 1913, MNRAS, 73, 359
Edge A., Sutherland W., Kuijken K., Driver S., McMahon R., Eales S., Emerson J. P., 2013, The Messenger, 154, 32
Flesch E. W., 2021, preprint (arXiv:2105.12985)
Foster C. et al., 2021, Publ. Astron. Soc. Aust., 38, e031
Gaensler B. M., Landecker T. L., Taylor A. R., POSSUM Collaboration, 2010, Am. Astron. Soc. Meeting Abstracts, #215
Gordon Y. A. et al., 2017, MNRAS, 465, 2671
Gürkan G. et al., 2015, MNRAS, 452, 3776
Gürkan G. et al., 2018, MNRAS, 475, 3010
Gürkan G. et al., 2019, A&A, 622, A11
Gürkan G., Croston J., Hardcastle M. J., Mahatma V., Mingo B., Williams W. L., 2021, Galaxies, 10, 2
Hale C. L. et al., 2021, Publ. Astron. Soc. Aust., 38, e058
Hardcastle M. J., 2018, MNRAS, 475, 2768
Hardcastle M. J., Krause M. G. H., 2013, MNRAS, 430, 174
Hardcastle M. J. et al., 2016, MNRAS, 462, 1910
Hardcastle M. J. et al., 2019, A&A, 622, A12
Hartley P., Jackson N., Badole S., McKean J. P., Sluse D., Vives-Arias H., 2021, MNRAS, 508, 4625
Hay S., O'Sullivan J., Kot J., Granet C., 2006, in Lacoste H., Ouwehand L., eds, ESA SP-626: The European Conference on Antennas and Propagation (EuCAP 2006). ESA, Noordwijk, p. 663
Heald G. H. et al., 2015, A&A, 582, A123
Heywood I. et al., 2016, MNRAS, 460, 4433
Hopkins A. M., Afonso J., Chan B., Cram L. E., Georgakakis A., Mobasher B., 2003, AJ, 125, 465
Hotan A. W. et al., 2021, Publ. Astron. Soc. Aust., 38, e009
Hurley-Walker N. et al., 2017, MNRAS, 464, 1146
Ighina L., Belladitta S., Caccianiga A., Broderick J. W., Drouart G., Moretti A., Seymour N., 2021, A&A, 647, L11
Intema H. T., Jagannathan P., Mooley K. P., Frail D. A., 2017, A&A, 598, A78
Ishwara-Chandra C. H., Saikia D. J., 1999, MNRAS, 309, 100
Isobe T., Feigelson E. D., Akritas M. G., Babu G. J., 1990, ApJ, 364, 104
Johnston S. et al., 2007, Publ. Astron. Soc. Aust., 24, 174
Joseph T. D. et al., 2019, MNRAS, 490, 1202
Kaiser C. R., Dennett-Thorpe J., Alexander P., 1997, MNRAS, 292, 723
Kauffmann G. et al., 2003, MNRAS, 346, 1055
Kewley L. J., Groves B., Kauffmann G., Heckman T., 2006, MNRAS, 372, 961
Koribalski B. S. et al., 2020, Ap&SS, 365, 118
Lacy M. et al., 2020, PASP, 132, 035001
Laing R. A., Riley J. M., Longair M. S., 1983, MNRAS, 204, 151
Lan T.-W., Prochaska J. X., 2021, MNRAS, 502, 5104
Leahy D. A. et al., 2019, Publ. Astron. Soc. Aust., 36, e024
Liske J. et al., 2015, MNRAS, 452, 2087
Macfarlane C. et al., 2021, MNRAS, 506, 5888
Mancuso C. et al., 2017, ApJ, 842, 95
Mandal S. et al., 2021, A&A, 648, A5
Manolakou K., Kirk J. G., 2002, A&A, 391, 127
Martin C. et al., 2003, in Blades J. C., Siegmund O. H. W., eds, Proc. SPIE Conf. Ser. Vol. 4854, Future EUV/UV and Visible Space Astrophysics Missions and Instrumentation. SPIE, Bellingham, p. 336
Matthews A. M., Condon J. J., Cotton W. D., Mauch T., 2021, ApJ, 909, 193
Mauch T., Murphy T., Buttery H. J., Curran J., Hunstead R. W., Piestrzynski B., Robertson J. G., Sadler E. M., 2003, MNRAS, 342, 1117
McConnell D. et al., 2016, Publ. Astron. Soc. Aust., 33, e042
McConnell D. et al., 2020, Publ. Astron. Soc. Aust., 37, e048
McKean J. P. et al., 2021, MNRAS, 505, L36
Merloni A., Nandra K., Predehl P., 2020, Nat. Astron., 4, 634
Mingo B. et al., 2022, MNRAS, 511, 3250
Mohan N., Rafferty D., 2015, Astrophysics Source Code Library, record ascl:1502.007
Morabito L. K. et al., 2022, A&A, 658, A1
Norris R. P. et al., 2011, Publ. Astron. Soc. Aust., 28, 215
Norris R. P. et al., 2021, Publ. Astron. Soc. Aust., 38, e046
Ocran E. F., Taylor A. R., Vaccari M., Ishwara-Chand ra C. H., Prandoni I., 2020, MNRAS, 491, 1127
Ocran E. F., Taylor A. R., Vaccari M., Ishwara-Chandra C. H., Prandoni I., Prescott M., Mancuso C., 2021, MNRAS, 500, 4685
Pennock C. M. et al., 2021, MNRAS, 506, 3540
Planck Collaboration VI, 2020, A&A, 641, A6
Prandoni I., Gregorini L., Parma P., de Ruiter H. R., Vettolani G., Wieringa M. H., Ekers R. D., 2000, A&AS, 146, 41
Prandoni I., Gregorini L., Parma P., de Ruiter H. R., Vettolani G., Wieringa M. H., Ekers R. D., 2001, A&A, 365, 392
Prandoni I., Guglielmino G., Morganti R., Vaccari M., Maini A., Röttgering H. J. A., Jarvis M. J., Garrett M. A., 2018, MNRAS, 481, 4548
Regener V. H., 1951, Phys. Rev., 84, 161
Robotham A. S. G., Davies L. J. M., Driver S. P., Koushan S., Taranu D. S., Casura S., Liske J., 2018, MNRAS, 476, 3137
Sabater J. et al., 2021, A&A, 648, A2
Saripalli L., Malarecki J. M., 2015, Proc. Sci., Giant Radio Galaxies as Probes of the Large-Scale Structure. SISSA, Trieste, PoS#44
Seymour N. et al., 2020, Publ. Astron. Soc. Aust., 37, e013
Shabala S. S., Jurlin N., Morganti R., Brienza M., Hardcastle M. J., Godfrey L. E. H., Krause M. G. H., Turner R. J., 2020, MNRAS, 496, 1706
Shimwell T. W. et al., 2017, A&A, 598, A104
Shimwell T. W. et al., 2022, A&A, 659, A1
Shirley R. et al., 2021, MNRAS, 507, 129
Smith D. J. B. et al., 2021, A&A, 648, A6

Smith M. W. L. et al., 2017, ApJS, 233, 26
Smolčić V. et al., 2017a, A&A, 602, A2
Smolčić V. et al., 2017b, A&A, 602, A6
Swarup G., Ananthakrishnan S., Kapahi V. K., Rao A. P., Subrahmanya C. R., Kulkarni V. K., 1991, Curr. Sci., 60, 95
Taylor M. B., 2005, in Shopbell P., Britton M., Ebert R., eds, ASP Conf. Ser. Vol. 347, Astronomical Data Analysis Software and Systems XIV. Astron. Soc. Pac., San Francisco, p. 29
Tingay S. J. et al., 2013, Publ. Astron. Soc. Aust., 30, e007
Turner R. J., Rogers J. G., Shabala S. S., Krause M. G. H., 2018, MNRAS, 473, 4179
van Haarlem M. P. et al., 2013, A&A, 556, A2
Webster B. et al., 2021, MNRAS, 500, 4921
White R. L., Becker R. H., Helfand D. J., Gregg M. D., 1997, ApJ, 475, 479
Wilber A. G., Johnston-Hollitt M., Duchesne S. W., Tasse C., Akamatsu H., Intema H., Hodgson T., 2020, Publ. Astron. Soc. Aust., 37, e040
Williams W. L. et al., 2019, A&A, 622, A2
Willis A. G., Strom R. G., Wilson A. S., 1974, Nature, 250, 625
Willott C. J., Rawlings S., Blundell K. M., Lacy M., 1999, MNRAS, 309, 1017
Wilman R. J. et al., 2008, MNRAS, 388, 1335
Wright E. L. et al., 2010, AJ, 140, 1868

## SUPPORTING INFORMATION

Supplementary data are available at *MNRAS* online.

**ASKAP-G23-catalogue.fits**

Please note: Oxford University Press is not responsible for the content or functionality of any supporting materials supplied by the authors. Any queries (other than missing material) should be directed to the corresponding author for the article.

[1]*Thüringer Landessternwarte, Sternwarte 5, D-07778 Tautenburg, Germany*
[2]*CSIRO Space and Astronomy, ATNF, PO Box 1130, Bentley, WA 6102, Australia*
[3]*INAF-IRA, Via P. Gobetti 101, I-40129 Bologna, Italy*
[4]*Department of Physics, University of Wisconsin–Milwaukee, PO Box 413, Milwaukee, WI 53201, USA*
[5]*CSIRO Space and Astronomy, ATNF, PO Box 76, Epping, NSW 1710, Australia*
[6]*School of Science, Western Sydney University, Locked Bag 1797, Penrith, NSW 2751, Australia*
[7]*Department of Astronomy, University of Cape Town, 7701 Rondebosch, Cape Town, South Africa*
[8]*Inter-university Institute for Data Intensive Astronomy, Department of Physics and Astronomy, University of the Western Cape, Robert Sobukwe Road, 7535 Bellville, Cape Town, South Africa*
[9]*International Centre for Radio Astronomy Research (ICRAR), University of Western Australia, Crawley, WA 6009, Australia*
[10]*Centre for Astrophysics and Supercomputing, Swinburne University of Technology, Hawthorn, VIC 3122, Australia*
[11]*ASTRON: the Netherlands Institute for Radio Astronomy, PO Box 2, NL-7990 AA Dwingeloo, the Netherlands*
[12]*School of Physics and Astronomy, Monash University, Clayton, VIC 3800, Australia*
[13]*School of Natural Sciences, University of Tasmania, Private Bag 37, Hobart, TAS 7001, Australia*
[14]*Departamento de Astronomía, DCNE, Universidad de Guanajuato, Callejón. de Jalisco s/n, Guanajuato, CP 36023, Mexico*
[15]*Australian Astronomical Optics, Macquarie University, 105 Delhi Road, North Ryde, NSW 2113, Australia*
[16]*Department of Physics and Astronomy, University of Calgary, Calgary, AB T2N 1N4, Canada*
[17]*Center for Theoretical Physics, Polish Academy of Sciences, al. Lotników 32/46, PL-02-668 Warsaw, Poland*
[18]*International Centre for Radio Astronomy Research – Curtin University, 1 Turner Avenue, Bentley, WA 6102, Australia*
[19]*Shanghai Astronomical Observatory, Chinese Academy of Sciences, Nandan road 80, Shanghai 200030, China*
[20]*Key Laboratory of Cognitive Radio and Information Processing, Guilin University of Electronic Technology, Guilin 541004, China*

This paper has been typeset from a TEX/LATEX file prepared by the author.